PNNL-14091

Pacific Northwest
National Laboratory
Operated by Battelle for the
U.S. Department of Energy

Final Report on Materials Characterization for the Wetted Cathodes for Low-Temperature Aluminum Smelting Program

C. F. Windisch Jr.

October 2002

Prepared for the U.S. Department of Energy
under Contract DE-AC06-76RL01830

PACIFIC NORTHWEST NATIONAL LABORATORY
operated by
BATTELLE
for the
UNITED STATES DEPARTMENT OF ENERGY
under Contract DE-AC06-76RL01830

PNNL-14091

Final Report on Materials Characterization for the Wetted Cathodes for Low-Temperature Aluminum Smelting Program

C. F. Windisch Jr.

October 2002

Prepared for
the U.S. Department of Energy and
Northwest Aluminum Technologies, Inc.
under Contract DE-AC06-76RL01830

Pacific Northwest National Laboratory
Richland, Washington 99352

Executive Summary

Cathode samples that were subjected to electrolysis testing by Northwest Aluminum Technologies, Inc. (NAT), Seattle, using a novel low-temperature reduction cell, were characterized at Pacific Northwest National Laboratory (PNNL) with optical microscopy, scanning electron microscopy (SEM), and energy dispersive x-ray spectroscopy (EDS). The principal focus of the analysis was determining the extent of degradation the samples had undergone, the characteristics of the aluminum metal layer that coated the cathodes, and the identity of reaction phases within and on the outside of the cathode material. Results of the materials characterization work performed at PNNL are reported in this document. The report entitled, *Final Report: Wetted Cathodes for Low-Temperature Aluminum Smelting* (DOE/ID-13901), written by the research team at NAT, covers details on reduction cell design, operation, and cathode performance, including a summary of the materials characterization results reported here.

Twenty-one cathode samples were delivered to PNNL from NAT, and 20 of these were analyzed at PNNL. One cathode from the 21 received was a duplicate and was not analyzed. A combination of optical microscopy, SEM, and EDS was applied to all cathode samples. The principal conclusions from this analysis were as follows:

- Very little corrosion of the cathode materials occurred in any of the samples.
- In most cases where some corrosion was observed, the corrosion mechanism appeared to be mainly intergranular corrosion. Only the top few layers of grains of cathode material were usually affected.
- Several of the samples showed higher wear at the corners, suggesting higher current densities at these locations.
- Different cathode compositions behaved slightly differently, although, as indicated above, none exhibited excessive wear. For example, cathodes containing Al_2O_3 appeared to degrade partly by reduction of some of the oxide to Al metal. Phases containing Zr also appeared to be more susceptible to reaction. The occurrence of intergranular corrosion suggests that impurities at grain boundaries (such as Ti and W, in reduced or elemental form, which were identified near grain boundaries by SEM/EDS) may influence this type of corrosion. Although the techniques employed were not sensitive enough to identify these impurity-mediated effects without ambiguity, it is possible that metallic (or reduced) impurities alloy with the aluminum metal upon wetting, resulting in loosened grains and accelerated transport of aluminum along grain boundaries.
- Al metal wetted the cathode materials very well in all cases. The thickness of the Al layer varied from sample to sample and also along the surface of an individual sample. Intact, uniform, and unbroken layers of Al on the order of 10 microns thick were measured in many cases.

Acknowledgments

This work was supported by the Office of Industrial Technologies, U. S. Department of Energy. The author acknowledges the technical assistance of Nat Saenz, Shelly Carlson, and James Coleman and the editorial assistance of Sheila Bennett, all of PNNL, as well as the programmatic support of Craig Brown at NAT. Pacific Northwest National Laboratory (PNNL) is operated by Battelle for the U.S. Department of Energy under Contract DE-AC06-76RL01830.

Contents

1.0 Introduction

The objective of this project was to perform post-test characterization of cathode samples that were subjected to electrolysis testing by Northwest Aluminum Technologies, Inc. (NAT), Seattle, WA. The electrolysis tests were performed in a novel low-temperature cell for smelting aluminum metal that is being developed by NAT with funding from the Office of Industrial Technologies, U.S. Department of Energy.

Cathodes in this cell design were in the form of small, thin plates. After testing, the plates were sent to Pacific Northwest National Laboratory (PNNL), where they were mounted, cross sectioned, and polished. A combination of optical microscopy, scanning electron microscopy (SEM), and energy dispersive x-ray spectroscopy (EDS) analysis was then performed on them to determine the extent of degradation the samples had undergone, the characteristics of the Al metal layer that coated the cathodes, and the identity of reaction phases within and on the outside of the cathode material. Results of the materials characterization work performed at PNNL are reported in this document. The report entitled, *Final Report: Wetted Cathodes for Low-Temperature Aluminum Smelting* (DOE/ID-13901), written by the research team at NAT, covers details on reduction cell design, operation, and cathode performance, including a summary of the materials characterization results reported here.

Section 2 describes results of this research. The figures discussed in Section 2 are included in an appendix at the end of the report. Conclusions are presented in Section 3.

2.0 Results

A list of all of the cathode samples received by PNNL is given in Table 2.1. The identifying information for each cathode sample that is given in this table is taken from sample labels and communications with NAT. Incomplete entries and notation clarification may be obtained directly from NAT and their final report on this project, *Final Report: Wetted Cathodes for Low-Temperature Aluminum Smelting* (DOE/ID-13901). Each cathode sample has an identification number assigned by NAT and by PNNL. The PNNL designations are used for the balance of this report. Readers can cross reference sample identities by referring to Table 2.1.

Table 2.1. List of All the Cathode Samples Studied in This Work

Cathode Sample (PNNL #)	Cathode Sample (NAT#)	Composition	Fabrication	Manufacturer	Test Conditions and Other Information	Month Analyzed at PNNL
NAT-1	None	TiB_2-Al_2O_3	P2C consolidated at 1800°C for 10 minutes	MMI	None (control)	4/01
NAT-2	None	TiB_2	P2C consolidated at 1800°C for 10 minutes	MMI	None (control)	4/01
NAT-3	None	TiB_2	P2C consolidated at 1800°C for 10 minutes	MMI	None (control), pre-mounted duplicate of NAT-2, not analyzed	4/01
NAT-4	#6	TiB_2	Hot pressed	Ceradyne	Four tests, each involving about 120 minutes of heatup and five hours of electrolysis with a cathode current density of 0.4 A/cm^2, followed by removal from the cell into air and cooling at room temperature	5/01
NAT-5	#188	TiB_2	Hot pressed	Ceradyne	Same as NAT-4 except several five-hour electrolysis tests prior to the final use	5/01
NAT-6	#12	TiB_2	P2C consolidated	MMI		6/01
NAT-7	#17	TiB_2-Al_2O_3 (10 v/o)	P2C consolidated (1900 C, 10 min, 30 MPa)	MMI		8/01
NAT-8	#20	TiB_2-ZrO_2		MMI		9/01
NAT-9	#26	TiB_2	Hot pressed		OIT/C 78,82,86,90	10/01
NAT-10	#32	ZrB_2	Hot pressed	MMI	Cathode C4(MMI)-HP	12/01
NAT-11		TiB_2			Ran 67 hr, OIT 951 10-7-01	12/01
NAT-12	#39	TiB_2		Ceradyne	OIT/(12) 12-18-01, 40 hrs.	2/02
NAT-13	#41	TiB_2		Ceradyne	OIT/C 129, 20 hrs.	2/02
NAT-14	#35	TiB_2-Al_2O_3	Hot pressed		OIT/C (HP)	2/02
NAT-15	#44	B_4C-TiB_2 (2.5-97.5)			Sample 2-3, 508, OIT/C132, 20-hr run	4/02
NAT-16	#45	B_4C-TiB_2 (10-90)			Sample 2-4, 511, OIT/C133, 20-hr run	4/02
NAT-17	#49	TiB_2-BN (97.5:2.5 w/o)			Sample 1-1, OIT-C 137	5/02
NAT-18	#51	TiB_2-BN (90:10 w/o)			Sample 1-4, OIT-C 139	5/02
NAT-19	#52	TiB_2-TiC (97.5:2.5 w/o)			Sample 3-2, OIT-C 140	5/02
NAT-20	#53	TiB_2-TiC (90:10 w/o)			Sample 3-4, OIT/C 141	5/02
NAT-21		Borided Ti metal	Ti metal implanted w/B		Not tested	9/02

2.1 NAT-1 and NAT-2

NAT-1 was found to consist primarily of three phases. It also contains pores. The primary matrix phase is TiB_2. A second phase looked like pores in the SEM backscatter mode but was actually found to be another phase. This second phase contains mostly Al and O, probably Al_2O_3. There is also a third phase scattered through the sample, mainly on the edges of real pores, sometimes filling them, and also, apparently, at some grain boundaries. This third phase appears metallic and contains mainly Fe, Ni, Cr, and Co.

NAT-2 has three phases and contains pores also. The first phase was identified as TiB_2, similar to NAT-1. A second phase is also present, uniformly scattered through the sample, between the grains of TiB_2 and at grain boundaries. It appears metallic and contains almost all Ti. The lack of other EDS peaks, including O and B (very weak but still observed for the major phase), suggests the phase is mainly metallic Ti. Some C is seen with the EDS but no more than observed for other regions of the sample, indicating it is not a carbide. Similar to NAT-1, there is also a minor phase, particularly near the pores, containing Fe, Ni, Cr, and Co.

In the appendix, Figures A.1 through A.3 show optical microscope images of NAT-1 and NAT-2 at different magnifications. Figure A.4 shows an optical micrograph of an uncut edge of NAT-2, demonstrating there are no significant reaction layers on the surface of the control materials. Figures A.5 and A.6 are SEM images of NAT-1 showing the principal phases. Figure A.7 is a labeled SEM image of NAT-2.

2.2 NAT-4

As shown in the macroscopic cross section in Figure A.8, overall material integrity is excellent. Corners remained sharp. The Al metal coated the surface very well. The thickness of the Al coating ranged from about 785 μm, where it appeared to accumulate as a "drip" near the bottom of the electrode, to about 25 μm farther up the sides (Figure A.9). At higher locations, the layer was even thinner and also appeared discontinuous in some places. Because these discontinuities did not appear to be accompanied by any particular wear of the TiB_2 at these locations, it is probable that they do not indicate persistent holes in the Al during electrolysis. More likely they are due to peculiarities associated with Al draining toward the upper parts of the electrode or "pull-out" during sample preparation. It may reflect the difficulty in maintaining an Al film intact during removal from the cell and sample preparation when the dimensions of the film are on the order of the grain size of the TiB_2. The TiB_2 grains are 10–20 μm and, as shown in Figure A.9, are very well wetted by the Al. The Al metal can be seen to penetrate into very small gaps created by the irregular grain geometries without any indication of a contact angle or other surface tension-related characteristics. Future work will focus more on the integrity of the Al layer as a function of distance from the bottom of the electrode.

Using SEM, the TiB_2 material showed very few signs of attack. A very slight amount of intergranular corrosion appears to have occurred but is largely limited to the first few layers of grains, on the order of 10–20 μm.

As shown in Figure A.10, the corner of the sample remained relatively sharp. Slightly more intergranular attack is visible at the corners (than at the sides) under SEM, but the total amount is still small, on the order of 10 μm or so.

Close inspection of the TiB_2 material (both bulk and near the surface) with SEM and EDS showed that it was composed of more than one TiB_2 phase that differed by varying small amounts of W (Figure A.11). W concentrations were on the order of 0.1 atom percent. The presence of W was unexpected. A few small Ti-containing regions also appeared metallic.

SEM/EDS of regions right at the Al/TiB_2 interface (Figure A.11) showed the presence of both Al metal and Al fluorides within the grain boundary cracks. Again, it should be emphasized that these cracks are essentially limited to the first few layers of grains. The presence of fluorides, however, suggests that even this small amount of corrosion might be lessened if procedures were changed to reduce contact time between the TiB_2 and the fluoride melt, e.g., by precoating with Al metal. For this sample, the grain boundary cracks occurred through the phase that is richer in W.

Some regions of the TiB_2 right near the surface contained a small amount of Al (about 1 atom percent), suggesting some slight solubility of Al in the TiB_2. The Al metal contains a significant amount of an Al-Fe-Si-Cu phase that coats the Al grains (Figure A.12). Presumably this phase is due to deposition of anode components that are dissolved in the melt. Careful analysis of the Al metal right near the Al/TiB_2 interface shows regions that are rich in Ti along with other metals such as Si, Fe, Cu and W. These regions appear metallic and suggest some slight amount of TiB_2 reaction, including reduction of Ti.

Optical microscopy was applied down the whole length of the sample to ascertain the integrity and thickness of the Al layer across its entire length. Previously, it was thought that in some regions the Al layer was not intact, but this was proven not to be the case upon closer scrutiny. Part of the problem with this analysis is that the Al layer is as thin as 10 μm in some locations, and the length of the specimen is 1-1/4 inch. Consequently, numerous photographs need to be taken at the appropriate magnification to resolve the complete Al layer over its entire length.

Figure A.13 shows the Al layer over its thinnest region on the sample. The top of the Al layer is about 17.4 mm from the bottom of the cathode. The picture shows the top approximately 6.8 mm length of this layer. Below the region shown, i.e., between the 10.6-mm mark and the bottom of the cathode, the Al is thicker and there are clearly no breaks in the Al layer. As shown in Figure A.13, 16 images were taken to illustrate the Al layer over its thin region (join B-to-B, C-to-C, etc.). In this region the layer is approximately 30 μm thick on average, but as thin as 10 μm in some regions, and thickens to about 65 μm near the 10.6-nm mark. Two important observations are noted:

1. There are no breaks in the Al. The Al layer is intact over its full length. In some regions, a few grains of the TiB_2 matrix have loosened and are floating in the Al layer, but the Al is still apparently unbroken by these grains.

2. The Al appears to wet the TiB_2, as well as any loose grains, down to at least 1-μm scale. Future work on other samples will include diagnostics of the Al layer over its full length, similar to the analysis reported here.

2.3 NAT-5

Overall material integrity of the TiB_2 is excellent, similar to NAT-4. However, significantly more rounding of the corners occurred, as shown in the macroscopic image in Figure A.14. Al coated the surface well. Thickness of the Al layer ranged from about 275 μm to 60 μm or less. Wetting was good and, as shown in Figure A.15, similar to NAT-4.

The mode and extent of attack of the TiB_2 appeared similar to NAT-4, with the top few layers of grains showing intergranular corrosion. Unlike NAT-4, the bulk TiB_2 had no detectable W. Some metallic Ti appeared to occur between grains, consistent with analysis of this type of material that was performed last year. Surprisingly, some Al was present in these metallic phases also, particularly near the surface of the material. In addition, the bulk TiB_2 contained Cr, about 0.2 atom percent in some locations. The characteristics of the corroded region were similar to NAT-4, with both Al metal and fluorides present in the cracks.

As shown in Figure A.16, some Ti-rich metal phases (Ti/Al ≈0.3) were observed in the Al metal near the surface of the electrode. The bulk Al phase also contained about 0.2 atom percent Ti, even far removed from the surface of the TiB_2.

2.4 NAT-6

The Al layer is intact and unbroken over the length of the cathode surface, as illustrated in the optical and SEM images in Figure A.17. However, the thickness of the Al varies along the length. It is several hundred microns thick where the Al is "balled up" near the bottom (B), and as thin as 10 microns in the middle area (C). The Al layer is also thicker farther up on the right side of the cross-sectioned sample. This thick portion of the layer covers and extends below a ledge on the right side surface of the TiB_2. It may be that this ledge inhibited draining of the Al to some extent, so the Al remained thicker in this region. Note also that the Al layer generally covered the bottom surface of the cathode well; however, the corners have little or no Al on them.

In addition to the good coating of Al on this cathode, there are several other similarities between NAT-6 and the cathodes analyzed previously. These include the intergranular attack of the TiB_2 matrix to a depth of about one layer of grains (C, D) and the observation of a metallic phase that contained anode components (e.g., Fe) along grain boundaries in the Al metal coating (see lighter phase in Al coating in B).

As shown in Figure A.18, the corner of cathode NAT-6 shows very little or no Al on it. This region of the cathode also shows slightly more intergranular attack, with eroded grain boundaries extending to a depth of another grain or two. Apparently, fluid dynamics in the cell keep the Al layer thin in this region and, coupled with the protection that the Al affords the TiB_2, may result in greater wear at the corners. In comparison, NAT-5 showed much more extensive wear at the corners. The phenomena at the corners of NAT-5 and NAT-6 appear to be related and suggest that cathodes will eventually show wear at sharp bottom corners, with the extent of this wear depending on cell operating conditions.

The SEM backscatter image in Figure A.18 also shows a white phase containing W (up to 30%) at the bottom surface of the cathode and extending a small distance up the sides. The presence of W will cause

a lightening in the SEM image, whether present in TiB_2 or in a separate metallic phase, because of its higher atomic number. So the phase could either be TiB_2 with significant W in it or a Ti-W metal alloy. Because our EDS detects boron as a small signal in TiB_2 and this boron signal is even weaker in the white region, it appears likely that the phase is, in fact, metallic. A metallic Ti phase, sometimes containing W, was also observed in the bulk of previous cathode materials (NAT-2, -4 and -5), so it is likely the W in this phase has a similar origin. Whether the apparent segregation of the W to the bottom surface of sample NAT-6 occurred during electrolysis or was a result of cathode fabrication is uncertain at this time.

Figure A.19 shows a higher magnification image in region C, previously shown in Figure A.17. Note that the Ti-W phase is also observed in this region. Again, the phase appears metallic. Its presence in the bulk, rather than on the surface, suggests that the phase, or at least the W component, was present as a result of fabrication conditions, not the electrolysis process.

2.5 NAT-7

Similar to all other previously tested anodes, the Al layer covering the anode is intact and essentially unbroken over most of the length of the cathode surface, as illustrated in the optical images in Figure A.20. Similar to other samples, the thickness of the Al varies along the length in a teardrop-like shape, thickest on the sides and very thin at the corners. The thickness is as great as 300 μm on the sides for this particular sample.

The surface of the cathode material was attacked significantly more in this study than in previous studies. As shown in the SEM image in Figure 21, several layers of grains were loosened from the matrix in NAT-7. This contrasts with the performance of NAT-6, where only the very top layer of grains was affected. The mode of attack appears to be intergranular corrosion, with the grains being loosened from the matrix while retaining much of their original geometric shape.

As shown in Figure A.21, the Al metal on NAT-7 has a second (lighter) phase distributed throughout, apparently coating grains of Al metal as they formed during quenching. Compared with the similar phase in the Al for NAT-6, this second phase is composed of anode components that dissolve and are reduced at the cathode along with the Al.

Higher magnification images of the Al/cathode interface (Figures A.22 and A.23) reveal part of the mechanism for intergranular attack in NAT-7. This cathode material has a phase of aluminum oxide, presumably Al_2O_3, distributed through it. As shown in Figure A.22, the oxide is missing in the intergranular region where Al metal has penetrated. Moreover, deeper in the cathode but still near the surface, the Al_2O_3 regions are partly eroded. Figure A.23 shows very high magnification images of two of these regions. EDS analysis reveals that the phase that (apparently) had once been Al_2O_3 now contains much less oxygen than the stoichiometric Al_2O_3 (as measured in regions further from the surface) as well as varying amounts of F, Na, and Ti. Clearly, there is some reaction that contributes to the deterioration of the Al_2O_3 phase near the surface of this cathode material. As the phase reacts the grains loosen, Al or electrolyte penetrates the cathode, and additional Al_2O_3 phase dissolves. It is likely that this mechanism involves cathodic reduction of the Al_2O_3 phase during cell operation, although it is unclear what roles the Al metal layer and the electrolyte play in this process.

As shown in Figure A.24, the bottom edge of the cathode also shows the same kind of degradation as the sides of the cathode. Surprisingly, the corners of the cathode are not as severely attacked. This is in contrast to other cathode materials where there was more extensive wear at the corners. This result may relate to the different behavior of the Al_2O_3 under different polarization conditions. Corners of the cathodes typically exhibit different current densities than the flat surfaces, so the conditions at the corners may be more favorable to the Al_2O_3 phase. Alternatively, the thinner Al layer at the corners may be beneficial to this phase. In any case, further study of the reactions of the Al_2O_3 phase appears warranted.

Electron dot maps appear to be useful in tracking interactions of the cathode and electrolyte, as shown in Figure A.25. Element distributions near the surface of NAT-7 indicate the presence of Al between the grains in the reacted region. Lack of large amounts of O (compared with O concentrations in the Al_2O_3 phase deeper in the matrix) suggests that most of this intruding Al is metallic. Also, the dot maps show significant penetration of F in regions where the Al_2O_3 has reacted, suggesting that electrolyte is somehow penetrating the cathode under the Al layer and that dissolution of the Al_2O_3 phase (into fluorides) may occur prior to electrolytic reduction of this phase.

One question that may arise is how the metallic Al or electrolyte penetrates the cathode material. This is particularly puzzling if the Al_2O_3 phase is widely distributed and isolated. For the material to undergo intergranular attack, as shown in Figures A.21 through A.25, some mechanism for transport along grain boundaries is required. Although analysis of grain boundary composition is more suited to TEM study, some line scans with EDS provide a clear, albeit less quantitative, explanation, as shown in Figure A.26. A line scan across a grain boundary that has not undergone corrosion shows evidence of the presence of Al. This means that either Al_2O_3 or Al metal exists as a thin layer along the grain boundaries. Given the reactivity of the Al_2O_3 phase observed in this work, it is likely that the phase along the grain boundaries is also aluminum oxide and that this phase contributes to the susceptibility of the cathode material to intergranular corrosion.

2.6 NAT-8

As shown in Figure A.27, the electrode material consists of TiB_2 with a secondary phase of ZrO_2. The ZrO_2 grains are on the order of 10 μm in size or smaller. EDS measurements showed trace amounts of Zr in the TiB_2 phase and higher amounts (6 at%) of Ti in the ZrO_2 phase.

The Al layer is essentially unbroken from the bottom of the cathode to about 8.9 mm from the bottom (position B in Figure A.28). In this region the layer shows the typical teardrop shape with a maximum thickness of about 300 μm. Above the 8.9 mm position there is an Al coating, but its thickness varies (between approximately 1 and 10 μm). It also appears discontinuous in some regions. Unless the cathode was only inserted to an 8.9-mm depth, these results mean that some upper (localized) portions of the material may not have been covered with Al and were exposed to the electrolyte.

As shown in Figure A.29, some of the ZrO_2 phase in the upper region appears to be attacked by the electrolyte. Figures A.2A and A.2B also show less ZrO_2 near the surface of the cathode than in the interior, a higher porosity, and grain separation, all suggesting some interaction between the ZrO_2 phase

and the electrolyte. It should be recognized, however, that a control electrode for this material was not studied, so the possible role of fabrication effects on ZrO_2 distribution has not been established.

The cathode material under the thicker Al layer at about 3.2 mm from the bottom (Figures A.28C and A.30) also shows evidence for some interaction with Al as well as reactivity of the ZrO_2 phase. Small amounts of metallic Al (containing Ti and Zr) were found in pores below TiB_2 surface. The TiB_2 phase near the surface also contained significant Zr, about 2 at%. This last result, along with the slight porosity and intergranular separation, may be consistent with the loss of ZrO_2 phase near the surface. Whatever the reason (either electrolysis or fabrication), the ZrO_2 may be reduced near the surface, creating voids and resulting in the doping of the TiB_2 phase with Zr.

As shown in Figures A.28D and A.31, the corner of this cathode was attacked more severely. The macro image in Figure A.2 shows significant rounding of the corners. SEM indicates that several layers of grains of TiB_2 are separated with an Al metal phase between them. The Al metal contains regions of metallic Ti/Zr, and there is a significant loss of the ZrO_2 phase near the surface.

The above results suggest that the ZrO_2 phase is susceptible to attack by electrolyte and/or aluminum metal, particularly at points of high current density, such as corners. However, it should be recognized that the dimensions of the cathode did not appear to vary dramatically except at the corners, indicating that once the ZrO_2 near the surface regions has reacted the electrode may stabilize, with a surface of largely TiB_2 protecting the rest of the material. Although this surface has pores and shows some intergranular separation, the ingress of electrolyte and/or aluminum metal may be slow enough that this material is not an unquestionably poor performer.

2.7 NAT-9

The material is hot-pressed TiB_2 that was tested in an electrolysis cell. Similar to NAT-8, the sample had a tab on the top of it for electrical connection. This tab was removed and the rest of it mounted and cross sectioned vertically down the center. The cross sections shown in this report are of this center region of the cathode, including the bottom edge, both sides, and up to the top just below the tab where the electrical connection was made. The “0” position is the bottom of the cathode. Key results are as follows.

Results were similar to other tested TiB_2 cathodes such as NAT-4, NAT-5, and NAT-6 that showed good wetting of the surfaces with Al metal. In the present sample, #26 (NAT-9), the Al appeared to coat both the bottom surface and the sides all the way up to the top of the cathode. The Al was largely intact over all these surfaces. Example SEM images at six different positions along the length of the cathode (as noted in Figure A.32) are shown in Figures A.33 through A.38.

The thickness of the Al layer varied from about 400 μm at the thickest portion in the center of the teardrop toward the bottom of the cathode down to less than 10 μm near the top. The thickness of the Al layer also varied in regions where it was thin and, in some areas, contained TiB_2 grains that had loosened from the matrix. At several positions, the size of these loosened grains was on the order of the thickness of the Al layer. Assuming the bottom corners of the cathode were originally sharp, significant rounding of these corners appeared to have occurred during testing. The Al layer coating these rounded corners was very thin, about 10 μm.

Results of chemical analysis (EDS) were similar to previous samples, showing Al metal and also some bath (fluoride) had penetrated the electrode along grain boundaries. Also similar to previous samples, the Al metal layer contained regions high in anode components such as Fe. Trace levels of Zr were also found near the bottom of the cathode.

2.8 NAT-10

SEM/EDS analysis of the bulk of this material (Figure A.39) confirmed that the matrix was composed of ZrB_2. However, small inclusions were also found within the bulk. Nominal composition of this phase was 51.5% Zr, 26% Fe, 17.5% U, and 5% Cr. No significant O was in this phase. Some B was found, but the amount scaled inversely with the size of the inclusion interrogated, suggesting the B was from the surrounding ZrB_2 phase. These results and the high contrast in the SEM (versus the ZrB_2 phase) suggest the inclusions are metallic.

As shown in Figure A.40, the Al metal coated both sides and the bottom of this sample. The Al was very thick in a few places, especially near the bottom, similar to observations in previous cathode samples. Instead of a teardrop shape, however, the Al had an unusually flat edge on one side of the sample (see the right side of the sample in Figure A.40). Under microscopic examination, the flat edge appeared to be due to a line of needle-like crystals that extended diagonally from the bottom edge of the sample. As shown in Figure A.41, these needles had the nominal composition Al_4W. They appeared to be metallic, suggesting they were an intermetallic composition of Al and W. (EDS analysis indicated an Al_4W stoichiometry, but it may be Al_5W, which is a known intermetallic composition.) There was also a thicker region of Al metal on the left side of the sample, about 15 mm up from the bottom. The Al thickness was almost 1 mm at its thickest point, on the right side of the sample near the bottom, and gradually thinned to about 10 μm further up. Very close inspection of the thinner regions revealed the coating had good integrity over the whole surface, although some small grains from the matrix were scattered throughout. The Al coating extended all the way up to the very top of the sample.

As shown in Figures A.40 (position A and C) and 41, thicker regions of Al were also found to contain aggregations of another material composed of Zr, B and O. This phase is probably a reaction product of the ZrB_2 and either Al metal or the molten salt. As shown in Figure A.41, grains of ZrB_2 were also loosened from the matrix by this interaction.

2.9 NAT-11

This sample had a curved bottom. SEM analysis (Figure A.42) revealed a fairly uniform and intact Al layer over both sides, all the way up to the top of the cathode. Thickness near the top was about 10 μm. On the inside of the curve near the bottom, the Al was thicker, approaching 150 μm.

Other than the intergranular corrosion described below, the extent of corrosion of the TiB_2 appears minimal, especially considering a 67-hour utilization time. Corrosion was observed only under microscopic examination.

As shown in Figure A.43 (thicker Al region), intergranular corrosion of the TiB_2 is evident within the first few layers of grains. Some loosened TiB_2 grains are also apparent within the Al layer. The mechanism for intergranular attack is not certain, but it is noteworthy that the TiB_2 grains within the matrix are characterized by an outer region (lighter in contrast in the SEM images) containing a significant amount of W. Closer to the surface, where intergranular attack had occurred, this W-containing phase is not as apparent. It may be that the W at or near the grain boundaries was more susceptible to attack than the TiB_2 matrix itself.

Within the Al metal, phases of Al-Fe-Ni-F and Al-Cu were also identified. The latter appears to be an intermetallic composition of Al and Cu.

2.10 NAT-12

SEM of this sample revealed that TiB_2 was the predominant phase. Some W was present in outer regions of the TiB_2 grains, however, appearing as a lighter gray phase in the micrographs. As shown in Figure A.44, there was very little wear of this sample as a result of testing. A few grains of TiB_2 can be seen in the Al layer (positions A and C, for example); however, there was very little, if any, intergranular attack that characterized previous samples. In the past, it was common to see at least the first layer of grains eroded around grain boundaries.

Unlike the cathode itself, the connector material (appearing as a rectangle toward the top of Figure A.44 macro image) showed significant intergranular corrosion. As shown in Figure A.45, there was high porosity and significant penetration of the Al into this material. Although the connector was composed of TiB_2, no significant amount of W occurred in this phase (unlike the cathode itself), suggesting the connector and cathode compositions were originally not the same. As shown in Figure A.44 position D, the Al metal also accumulated under the connector and penetrated the space between the connector and the cathode.

The Al layer was about 10 μm thick in most places over the surface of the cathode (Figure A.44 position C), except at the corners where it was thinner and on the sides near the bottom where it was somewhat thicker. There were also several places along the sides of the cathode that showed gaps in the Al layer (Figure A.44 position E and Figure A.46), but no additional corrosion of the cathode occurred in these places.

2.11 NAT-13

This sample showed a cathode secured “inside” a grooved connector, as shown in the macro image in Figure A.47. Analysis of the bulk of the cathode revealed TiB_2 grains with W present in the outer regions of these grains. At certain locations at grain boundaries, particles of Ti (presumably metallic) with other minor constituents were also present. As shown in Figure A.48, the composition of the connector material was similar.

As shown in Figures A.47 (positions A and C) and 49, there was a significant amount of intergranular corrosion of this material, both in the cathode and in the connector, particularly near corners. However,

even the sides of the cathode showed intergranular attack (Figure A.47 position C). Grains, several layers deep into the cathode, appear separated.

The Al layer along the surface of this sample showed widely varying thickness in the region that was sampled (Figure A.47 macro). Similar to NAT-12, the Al penetrated the space between the connector and the cathode and was present in spaces between separated grains as well (Figures A.47 position E and A.50). The Al in this region also contained black particles that were identified as carbon (Figure A.49).

2.12 NAT-14

This cathode was composed mainly of TiB_2 with a phase of Al_2O_3 distributed through it (Figures A.51 and A.52). The top several grains of the material showed intergranular corrosion (Figure A.51 positions A, C, D, and E), and numerous TiB_2 grains were floating in the Al layer. Unlike NAT-12 and NAT-13, the corners of NAT-14 were very round. Assuming the corners were initially sharp, this means there was a significant amount of corrosion of the corners during testing.

The Al metal layer was very thin, about 10 μm in most places (except near the teardrop at the bottom of the cathode). The Al also penetrated the cathode material where there was intergranular corrosion. It is not clear, however, whether the Al formed as a result of reduction of alumina originally dissolved in the melt or due to conversion of Al_2O_3 in the cathode itself. The SEM image in Figure A.52 highlights this ambiguity.

The bottom of this sample also showed several cracks that extended hundreds of microns up into the cathode. Al metal was detected in these cracks, indicating that they were present during electrolysis testing.

2.13 NAT-15

Both NAT-15 and NAT-16 were composite samples of TiB_2 and B_4C. The SEM micrographs in Figure A.53 show the microstructure of NAT-15. The B_4C phase appears as black regions, approximately 1-10 microns in size, in the backscattered electron image and is more clearly resolved in the secondary electron image. The difficulty in observing features in the B_4C phase in the backscattered electron image is due to the high contrast between the B_4C and the TiB_2 matrix. Nevertheless, the backscattered electron image shows better detail in other respects, including grain boundaries and reaction phases. Because samples were C-coated to minimize charging during SEM/EDS analysis, it was difficult to be quantitative, especially in high-carbon phases like B_4C. For this reason, the EDS results were not corrected for C coating. B-containing phases with high amounts of C were therefore assumed to be B_4C. Carbon in phases other that those containing significant amounts of B was assumed to arise from the C coating. The only exceptions to this were the large particles in the Al layer in NAT-16 that contained almost exclusively C (discussed below).

Careful analysis of the Al layer on NAT-15 showed that it was thin, mostly on the order of 10 μm, and that it varied in thickness along the length of the cathode. Toward the bottom of the cathode, the layer was on the order of 100 microns thick or more (Figure A.54 positions A and B), while farther up the

thickness was closer to 10 μm (Figures A.54 position D and A.55 position F). There were exceptions to this, however. Some locations had no observed Al layer (Figure A.54 position C), while some positions higher up the side of the sample had thicker layers (Figure A.55 position E).

The cathode material showed evidence of intergranular corrosion to a depth of only a few grains (Figures A. 54 and A.55). Corners were also fairly sharp, suggesting the extent of corrosion during this 20-hr test was minimal. Nevertheless, evidence for a small amount of interaction was observed. The intergranular corrosion was accompanied by some penetration of Al into the electrode material. (See, for example, phases labeled Y and Z in Figure A.54 position C.) Phase Y contained mostly Al and O but also significant amounts of F, Na, Ti, and Si. Phase Z, relatively deep within the material, contained mostly Al. Evidence for a reaction right at the Al/electrode interface was also observed. Figure A.54 (position A) shows a feathery phase at this interface, labeled X, composed of mostly Al and O but also Ti, Na, Cl, and W. The white phase on the boundary of the TiB_2, also at this interface, labeled TiB_2 + W + Mo, on the other hand, may be a remnant from cutting or grinding or other electrode preparation procedures.

The Al layer also contains some other phases. Particles of aluminum oxide, presumably Al_2O_3, were observed at high densities in a few locations (Figure A.54 position B). Grains of TiB_2, loosened from the matrix, were also apparent (e.g., Figure A.55 position F). Small particles of metallic phases high in Fe and Cu were also seen (e.g., Figure A.55, position E), similar to those observed on other cathodes.

It is also worth noting that regions where the Al layer was missing (Figure A.54 position C) did not show significantly more corrosion than regions covered by the Al. This may be because the regions were covered with Al during electrode operation, or it may result from the durability of this material even upon direct contact with the electrolyte. Finally, it is curious that no phases of B_4C were observed in the Al metal layer or outside of the electrode material. Although the amount of corrosion was comparatively small, it might have been expected that some of this phase, like the TiB_2, would have loosened from the electrode and ended up in the Al layer. But this was not the case. There are at least three possible reasons for this:

- The B_4C phase was unreactive.
- The B_4C phase was sufficiently remote from the original surface of the electrode that no interaction occurred within the time frame of the experiment.
- The B_4C completely reacted.

The latter does not seem likely because, as shown in Figure A.55 (position E), B_4C is clearly seen near the Al/cathode interface with no evidence of reacting. Regions around this B_4C particle (and probably accessible to it along grain boundaries) contain Al or other species from the electrolysis cell, yet the B_4C appears unaffected.

2.14 NAT-16

NAT-16 was compositionally similar to NAT-15 but contained more B_4C, as shown in Figure A.56. The B_4C phase also has a greater particle size distribution in this sample, with some locations as large as 50 μm or more.

The Al layer on NAT-16 was similar to that on NAT-15. Over the regions studied, it appeared more intact, however, with fewer gaps than observed on NAT-15. Intergranular corrosion was also observed on this sample, with the extent of corrosion slightly more severe than in NAT-15. (Compare Figures A.57 position A and A.54 position A, for example.) As shown in Figure A.57 (positions A, B, C, and D), essentially all the interactions described for NAT-15 were also observed for NAT-16. The Al layer also contained particles of Al_2O_3, TiB_2, and the metallic Cu/Fe phases, similar to NAT-15.

NAT-16 also showed the presence of a high-C phase in the Al layer (Figure A.57 positions B and C). This phase showed an extraordinarily high amount of C, more than attributable to the C coating but much less B than the B_4C phase. For this reason, we believe these particles to be essentially C. It is unclear where these C particles came from. Two possibilities are that they were present from sources other than the cathode itself or that they formed from some reaction involving the B_4C phase.

2.15 NAT-17, NAT-18, NAT-19, and NAT-20

Figure A.58 shows the macro optical images of cross sections of all four cathodes. All cathodes showed minimal wear at this low magnification. Corners remained relatively sharp (compared with results for some of the other cathodes). Also, as noted before, the Al metal appeared to wet the surfaces with thin films (although the details of the wetting may be different for the different cathodes, as described below) and also tended to form a teardrop shape at the bottom of each cathode, apparently due to the liquid Al solidifying in this shape as the cathode was removed from the electrolyte. Sample NAT-19 had an approximately 1.5-mm vertical crack extending up from near the center of the sample bottom.

As shown in Figure A.59, the bulk microstructures of the four cathodes were different. NAT-17 and NAT-18 contained different amounts of BN as a second phase, 2.5% and 10%, respectively. The BN was difficult to resolve using the backscattered electron SEM image, as illustrated for NAT-17 in Figure A.59. With backscattered electrons, the BN phase was too dark and resembled pores. Using the secondary electron image, however, as shown for NAT-18 in Figure A.59, the presence of a second phase, i.e., BN and not pores, was established. As expected, the area fraction of the BN phase was greater for NAT-18 than for NAT-17. EDS analysis of the BN phase was not quantitative. The presence of both elements, B and N, was established, consistent with BN, but quantification was difficult, especially due to the relatively poor sensitivity of the instrument to B. Measurements on the TiC-containing samples, NAT-19 and NAT-20, containing 2.5% and 10% TiC, respectively, were also qualitative. The second phase, TiC, was clearly identified, as shown in Figure A.59, with both backscattered and secondary electron images, and also exhibited a greater area fraction for NAT-20 than for NAT-19, as expected. However, similar to B, C is difficult to quantify in this case because it was also used to coat the samples with an electrically conductive layer prior to SEM. For this reason, the C content of the TiC phase was always higher than

the TiC stoichiometry. However, the C content of the TiC phase was always greater than the surrounding C-coated TiB_2 phase, which, combined with the higher Ti content and low B, was consistent with the presence of TiC.

As shown by the SEM images in Figure A.60, the corners of all four samples were relatively sharp. Samples NAT-17 and NAT-19, which had lower amounts of BN and TiC, respectively, than the other two samples, showed a marginally greater amount of rounding, but the differences seemed too small to be significant. Some intergranular corrosion is apparent for all four samples, but it occurred only to a depth of a few grains, which also may not be significant. Sample NAT-18 appeared to show the most noticeable intergranular attack, but again it was only a few grains deep. The microstructure of NAT-18 was somewhat different than that of the other two samples in this region, showing a more elongated TiB_2 phase, which may facilitate grain separation, although this is far from certain given the small amount of corrosion in all the samples. An apparent reaction product phase was also observed for samples NAT-17 and NAT-18, suspended in the Al metal. This phase was identified as nominally Ti_2Al. However, because it appeared in a powder-like form, the EDS analysis probably picked up additional Al from the surrounding Al metal, so the Ti content of the phase is probably higher.

Figure A.61 shows the Al layer on all four samples at distances above the bottom edges. The Al coatings on samples NAT-18, NAT-19, and NAT-20 were fairly uniform, with thicknesses on the order of 10 microns or less. Sample NAT-17, on the other hand, showed regions with minimal Al thickness, as shown in Figure A.61. These regions exhibited no additional corrosion, however, suggesting the Al had coated the surface during electrolysis and may have drained off upon removal from the electrolyte. The presence of a submicron layer of Al also cannot be discounted.

2.16 NAT-21

This sample was from a novel cathode formulation consisting of metallic Ti that had been implanted with B. The sample was not tested and was delivered to PNNL for analysis as a control sample prior to studying tested samples. As it turned out, the material did not perform well in electrolysis testing, and further use of it was abandoned. Nevertheless, the control sample that was received by PNNL was analyzed before this less-than-promising behavior was known.

As shown in Figure A.62, the material consisted of mostly metallic Ti with about 8 at% Al and also some V that occurred mainly in a second phase. As shown in Figure A.62, the implantation resulted in a thin layer of Ti-B compound, probably TiB_2 right at the surface. (Note that the B concentration is not certain because of the poor quantification of B in the EDS.) This Ti-B layer was not uniform and had breaks along its surface. Under the Ti-B layer, there was another thin, possible porous layer that was devoid of Al.

3.0 Conclusions

The principal conclusions from this analysis were as follows:

- Very little corrosion of the cathode materials occurred in any of the samples.
- In most cases where some corrosion was observed, the corrosion mechanism appeared to be mainly intergranular corrosion. Only the top few layers of grains of cathode material were usually affected.
- Several of the samples showed higher wear at the corners, suggesting higher current densities at these locations.
- Different cathode compositions behaved slightly differently, although, as indicated above, none exhibited excessive wear. For example, cathodes containing Al_2O_3 appeared to partly degrade by reduction of some of the oxide to Al metal. Phases containing Zr also appeared to be more susceptible to reaction. The occurrence of intergranular corrosion suggests that impurities at grain boundaries (such as Ti and W, in reduced or elemental form, which were identified near grain boundaries by SEM/EDS) may influence this type of corrosion. Although the techniques employed were not sensitive enough to identify these impurity-mediated effects without ambiguity, it is possible that metallic (or reduced) impurities alloy with the aluminum metal upon wetting, resulting in loosened grains and accelerated transport of aluminum along grain boundaries.
- Al metal wetted the cathode materials very well in all cases. The thickness of the Al layer varied from sample to sample and also along the surface of an individual sample. Intact, uniform, and unbroken layers of Al on the order of 10 microns thick were measured in many cases.

Appendix A

Images

Appendix A: Images

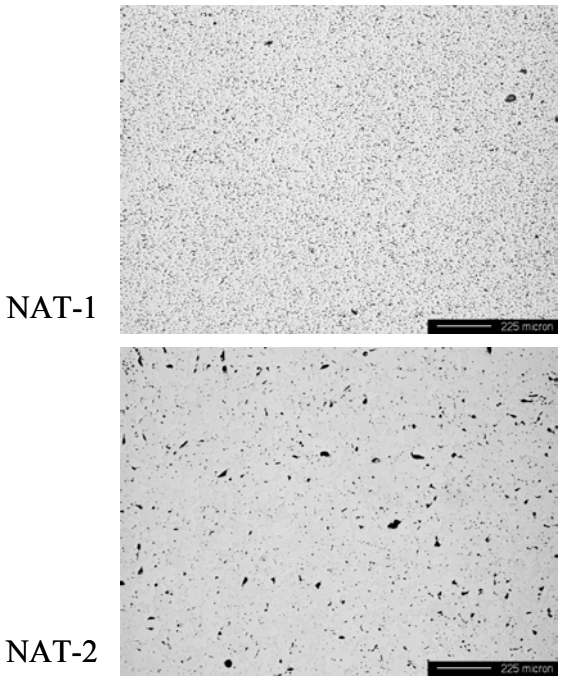

Figure A.1. Optical Microscopic Images of NAT-1 and NAT-2 at 50x Magnification

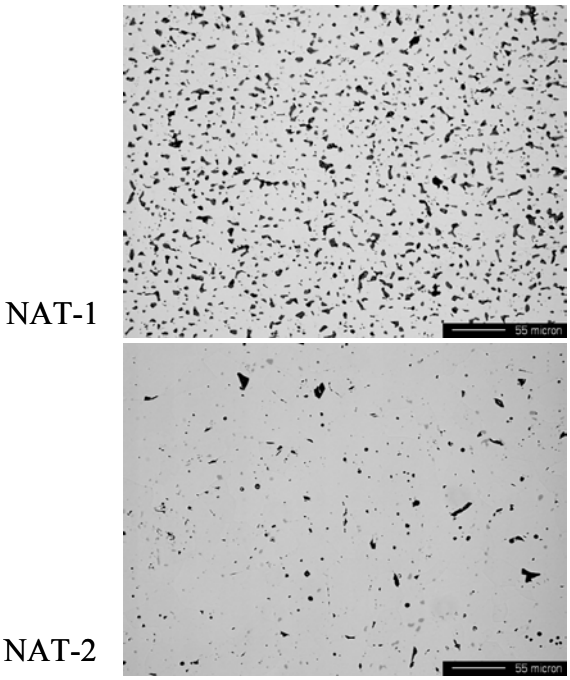

Figure A.2. Optical Microscopic Images of NAT-1 and NAT-2 at 250x Magnification

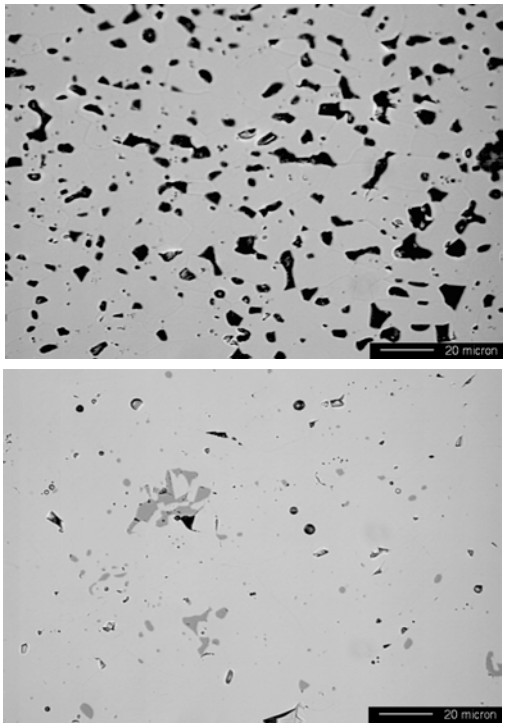

Figure A.3. Optical Microscopic Images of NAT-1 and NAT-2 at 500x Magnification

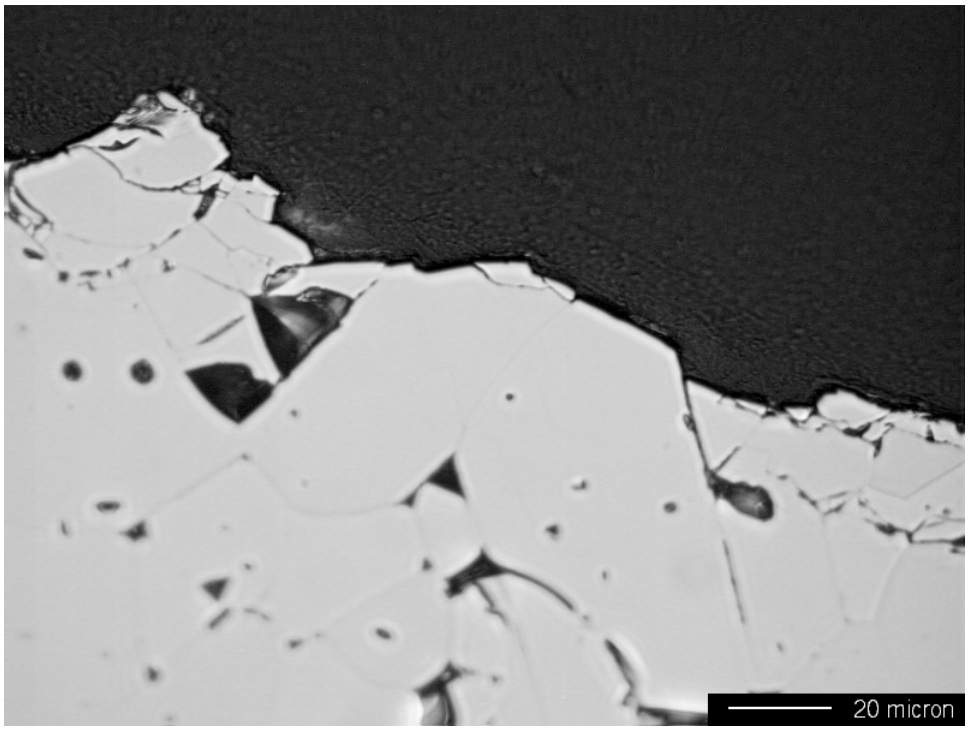

Figure A.4. Optical Microscopic Image at 500x Magnification of an Uncut Edge of NAT-2 Showing Absence of Reaction Layers

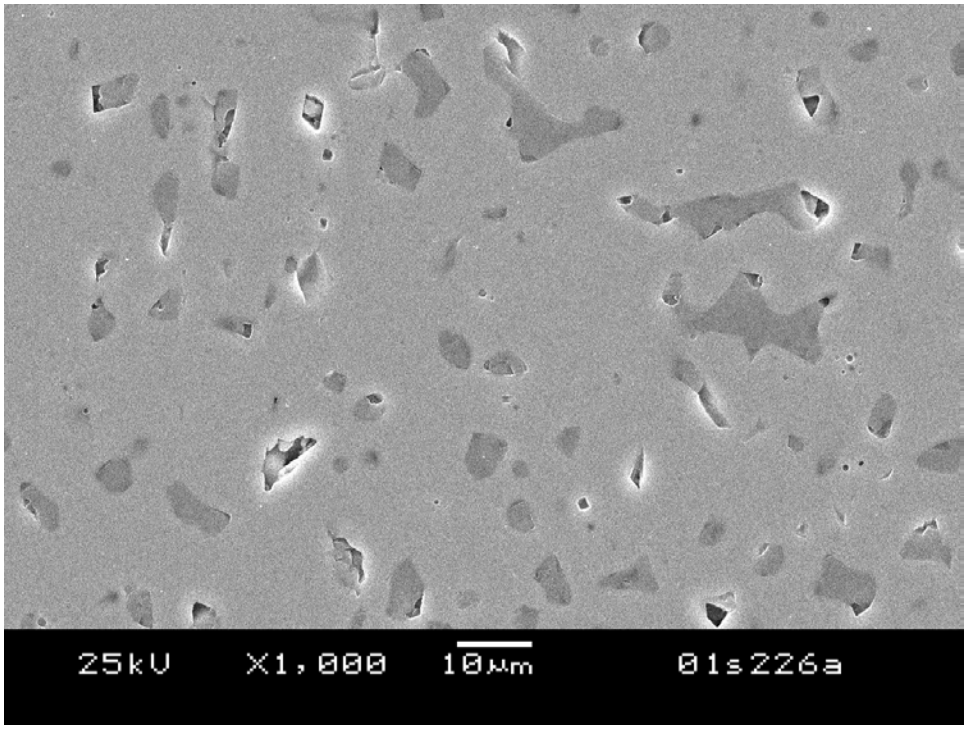

Figure A.5. SEM Image of NAT-1 Showing Principal Phases

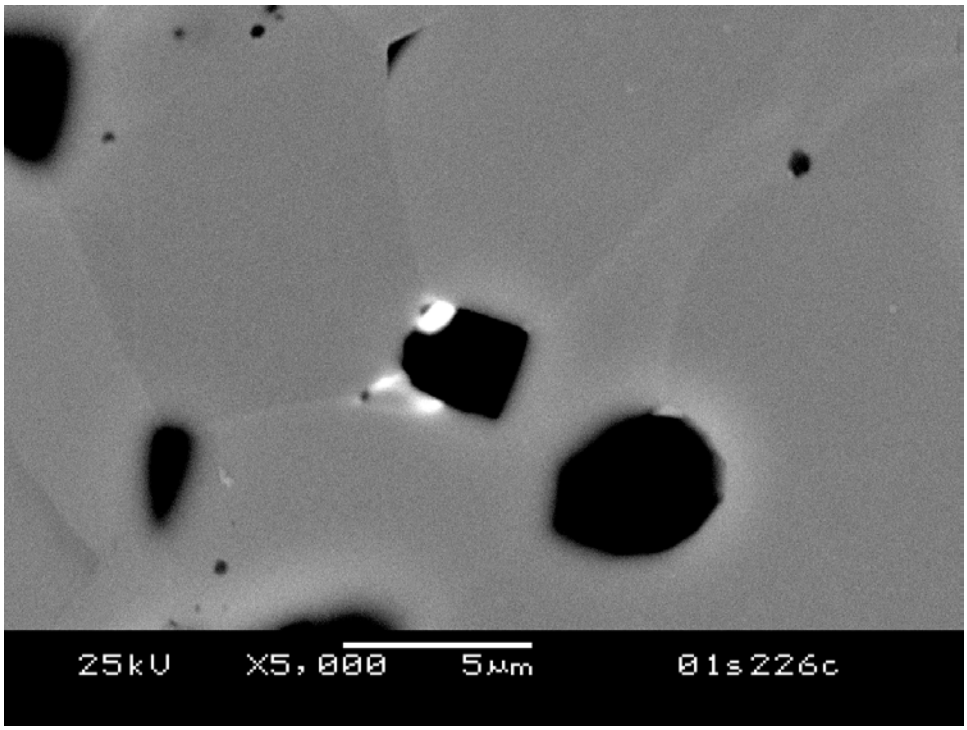

Figure A.6. SEM Image of NAT-1 Showing Additional Phases

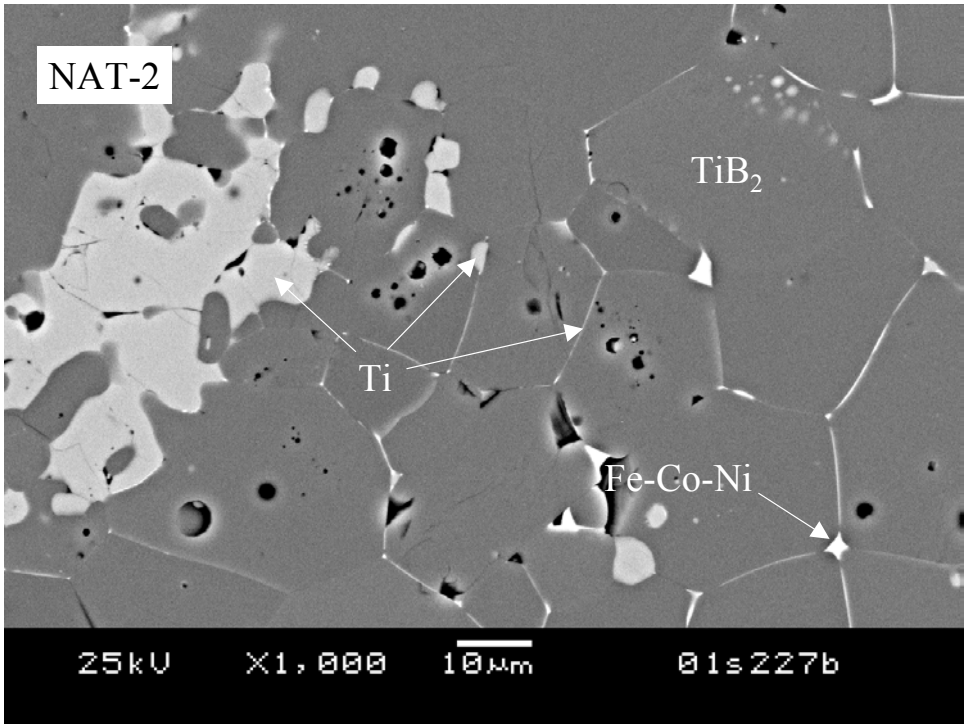

Figure A.7. SEM Image of NAT-2 Showing Principal Phases

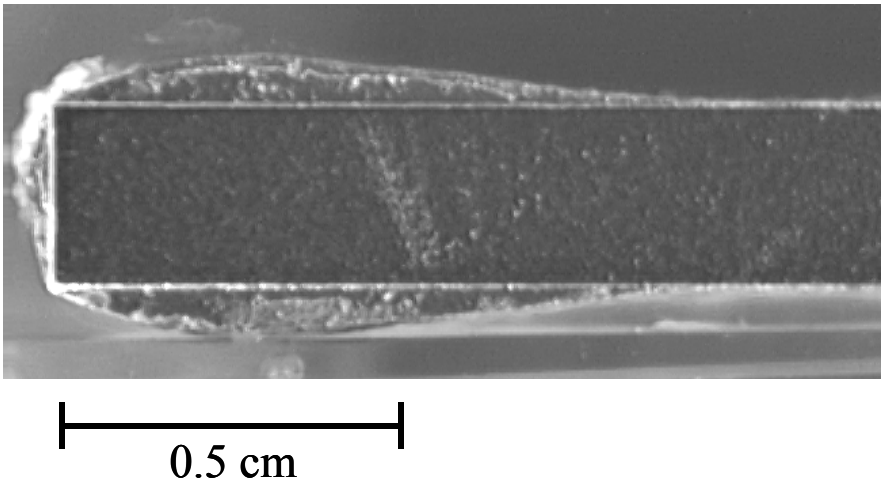

Figure A.8. Optical Image of Cross Section of NAT-4

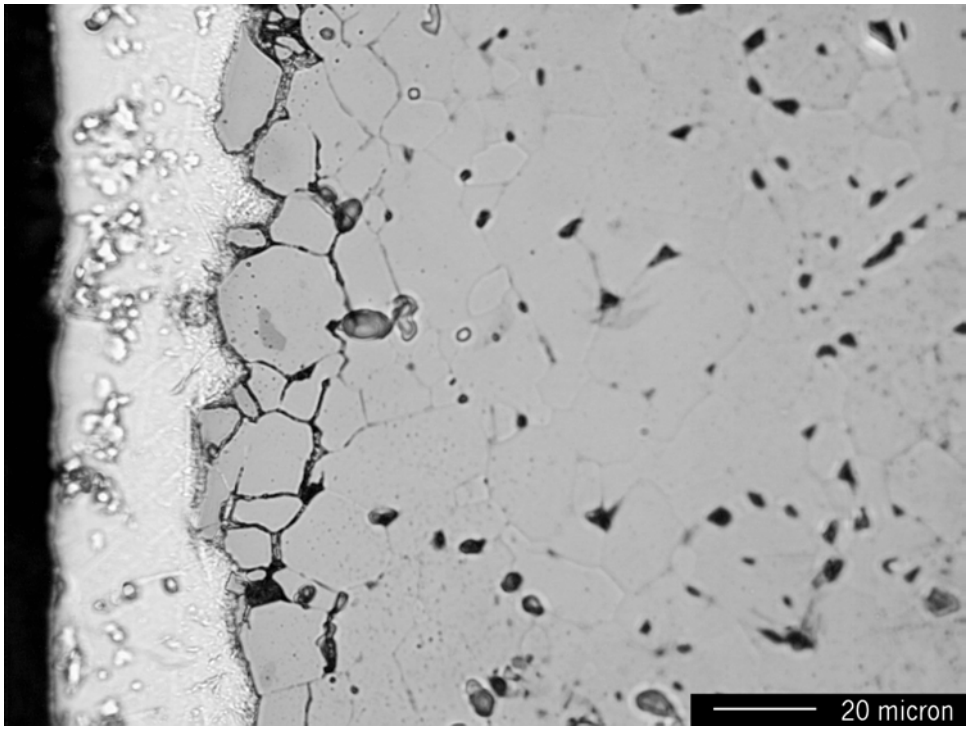

Figure A.9. Optical Microscopic Image of Al Layer on NAT-4 Approximately 25 μm from the Bottom Surface of the Sample

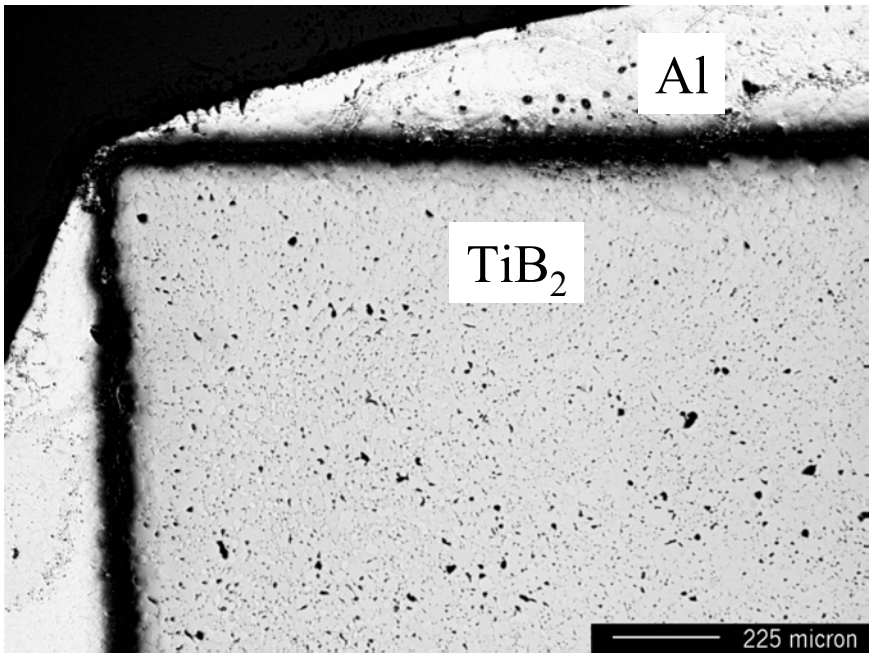

Note: Black band between TiB_2 and Al is a polishing artifact observed at this magnification.

Figure A.10. Corner of NAT-4

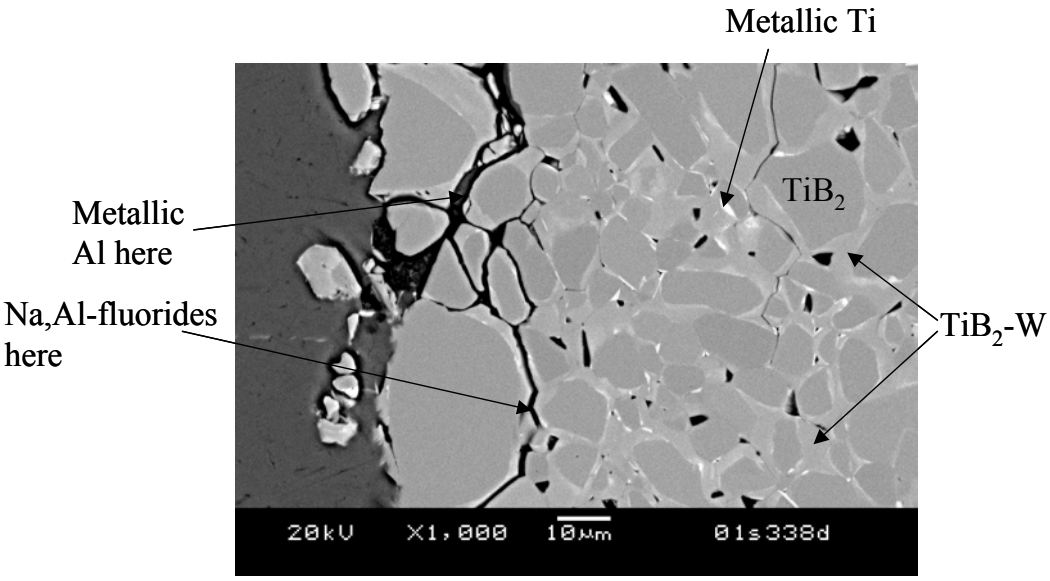

Figure A.11. SEM Image of NAT-4 Showing EDS Results on the Major Phases

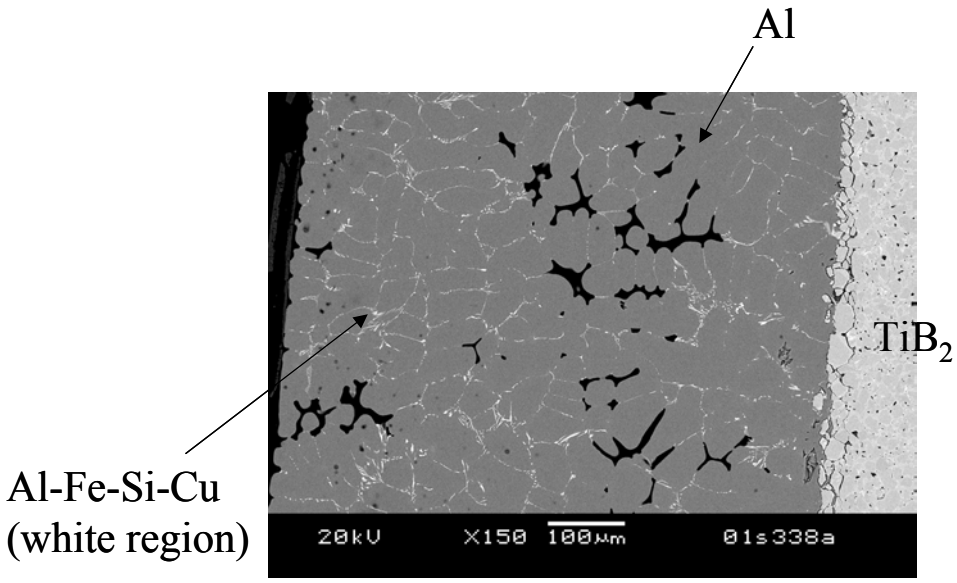

Figure A.12. SEM Image of Al Layer on NAT-4 with EDS Results

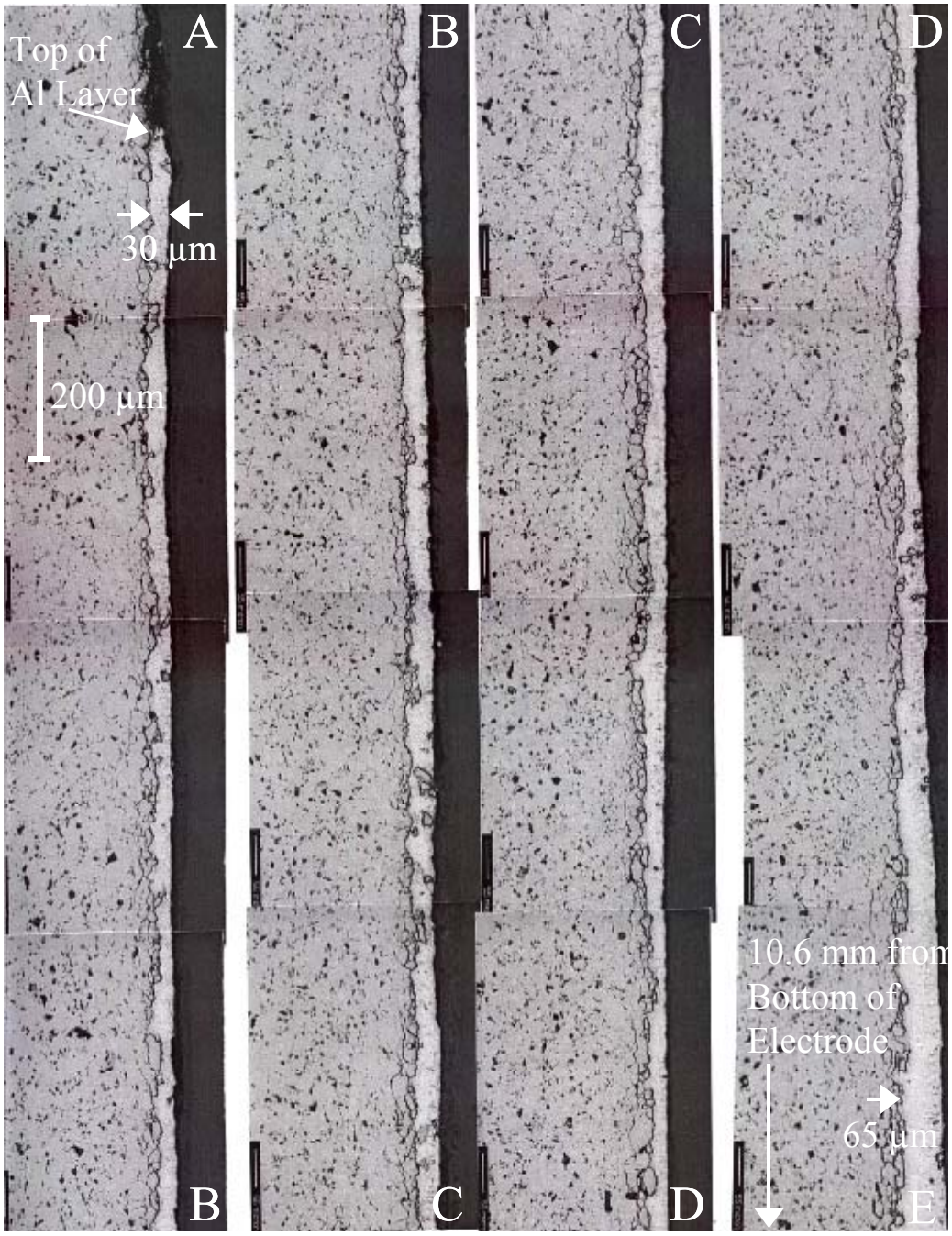

Figure A.13. Composite Optical Image Showing Al Metal Layer over Most of the Cathode Surface

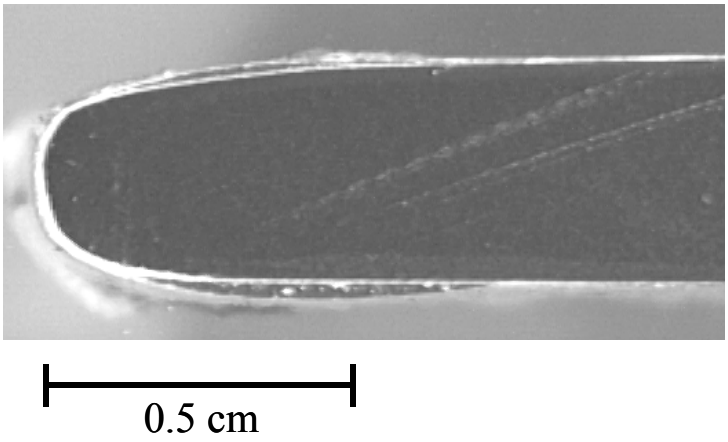

Figure A.14. Optical Image of Cross Section of NAT-5

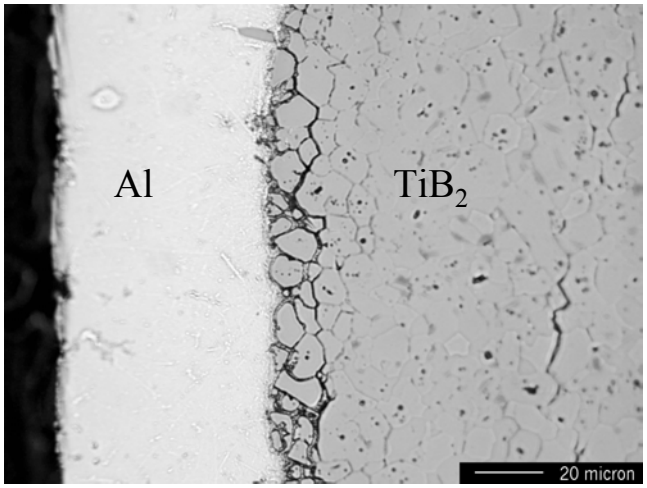

Figure A.15. Optical Microscopic Image of Al Layer on NAT-5

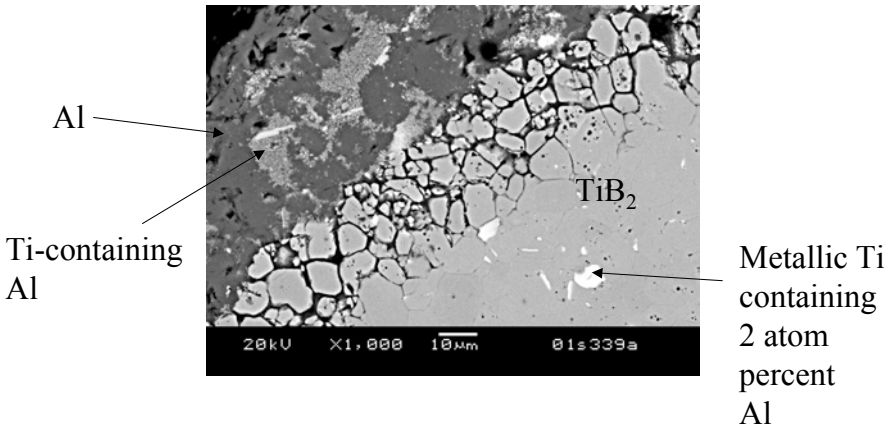

Figure A.16. SEM Image of Al Layer on NAT Showing Ti-Rich Metal Phases in the Al Metal

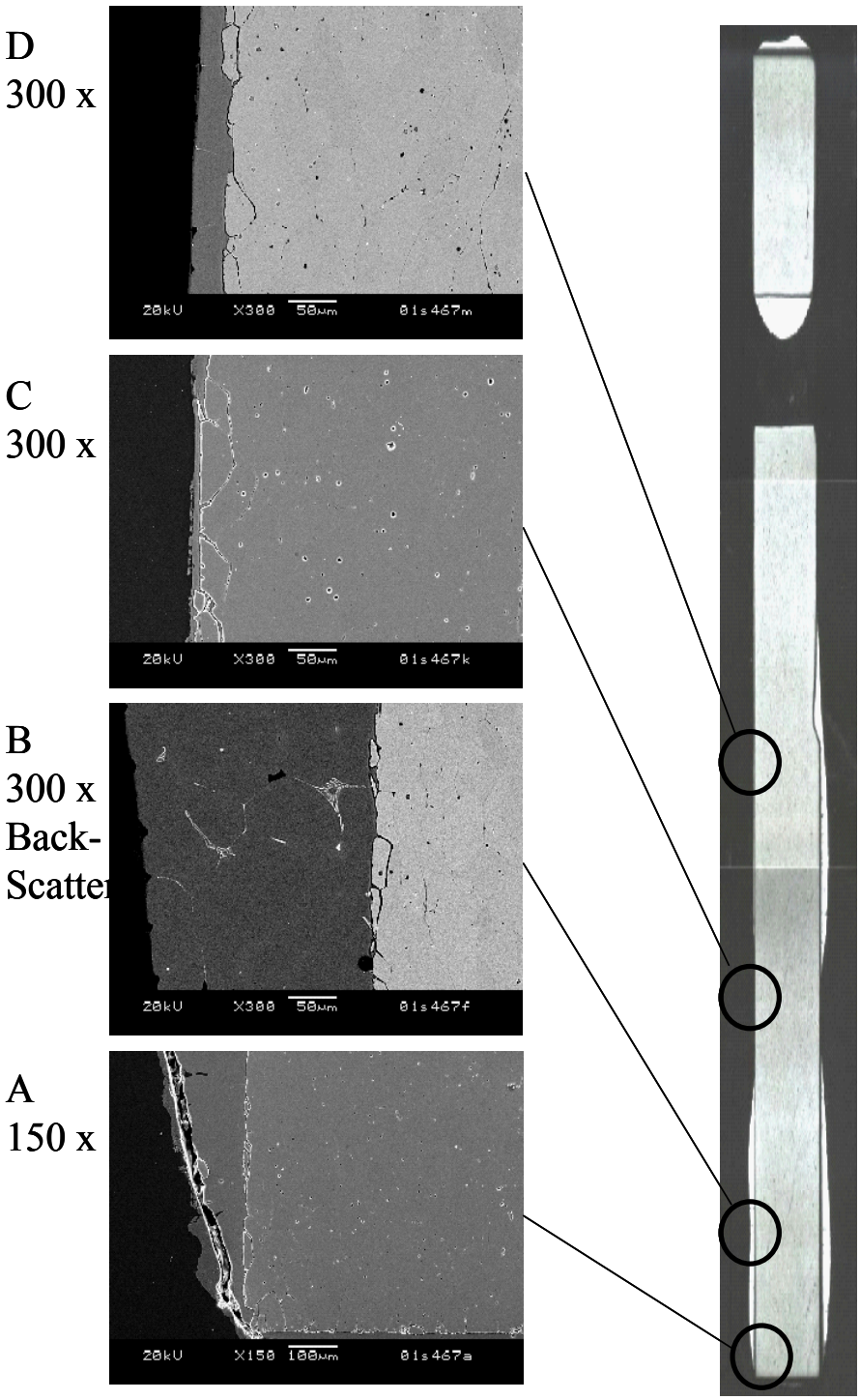

Figure A.17. Composite Optical Image of NAT-6 Cathode with SEM Images Showing the Al Layer at the Locations Noted

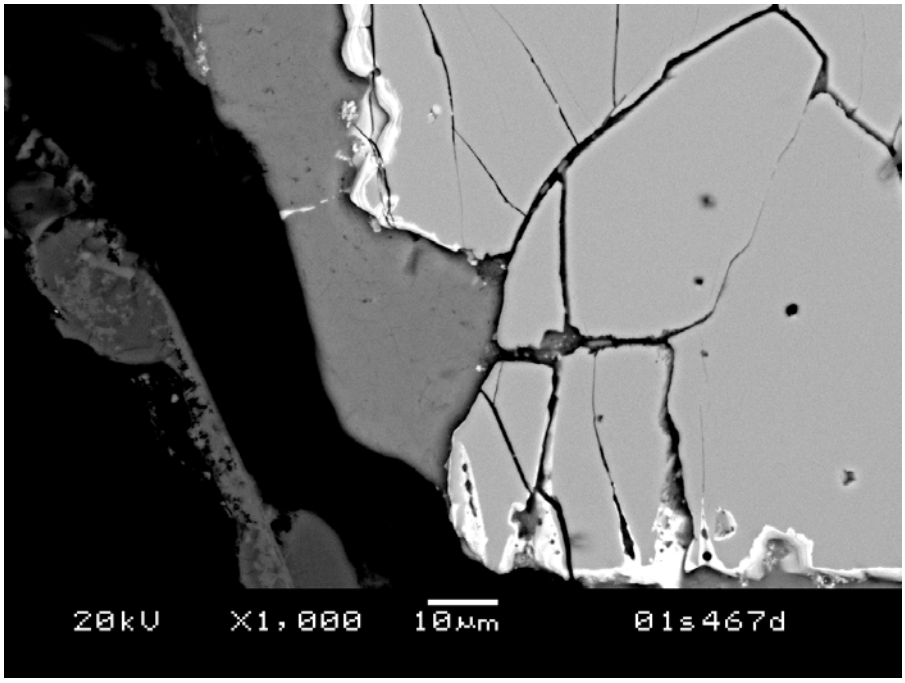

Figure A.18. SEM Image of the Corner of NAT-6 Showing Lack of Al on the Corner

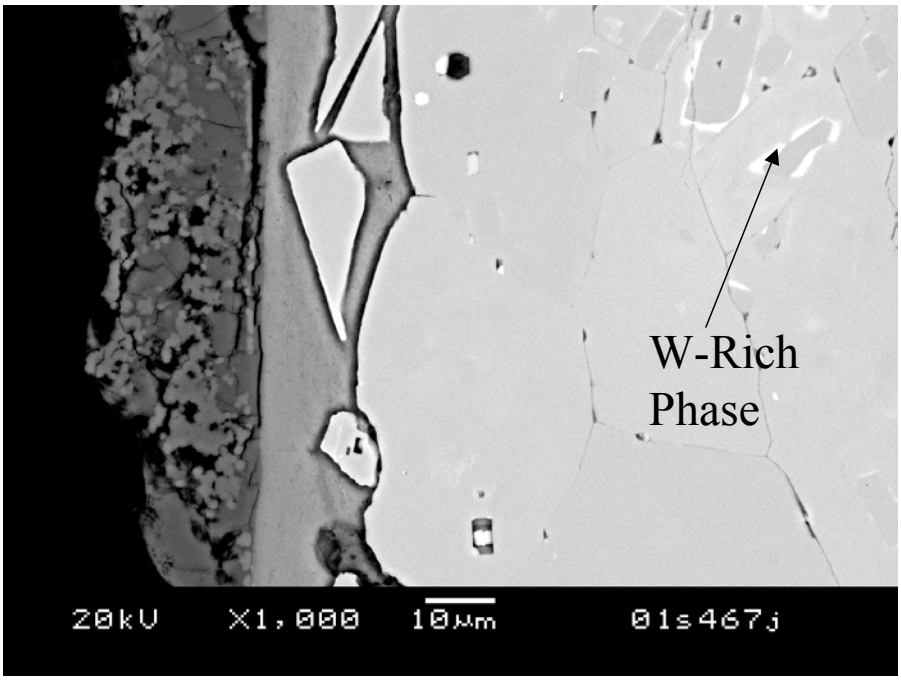

Figure A.19. SEM Image of NAT-6 Showing Presence of Ti-W Phase

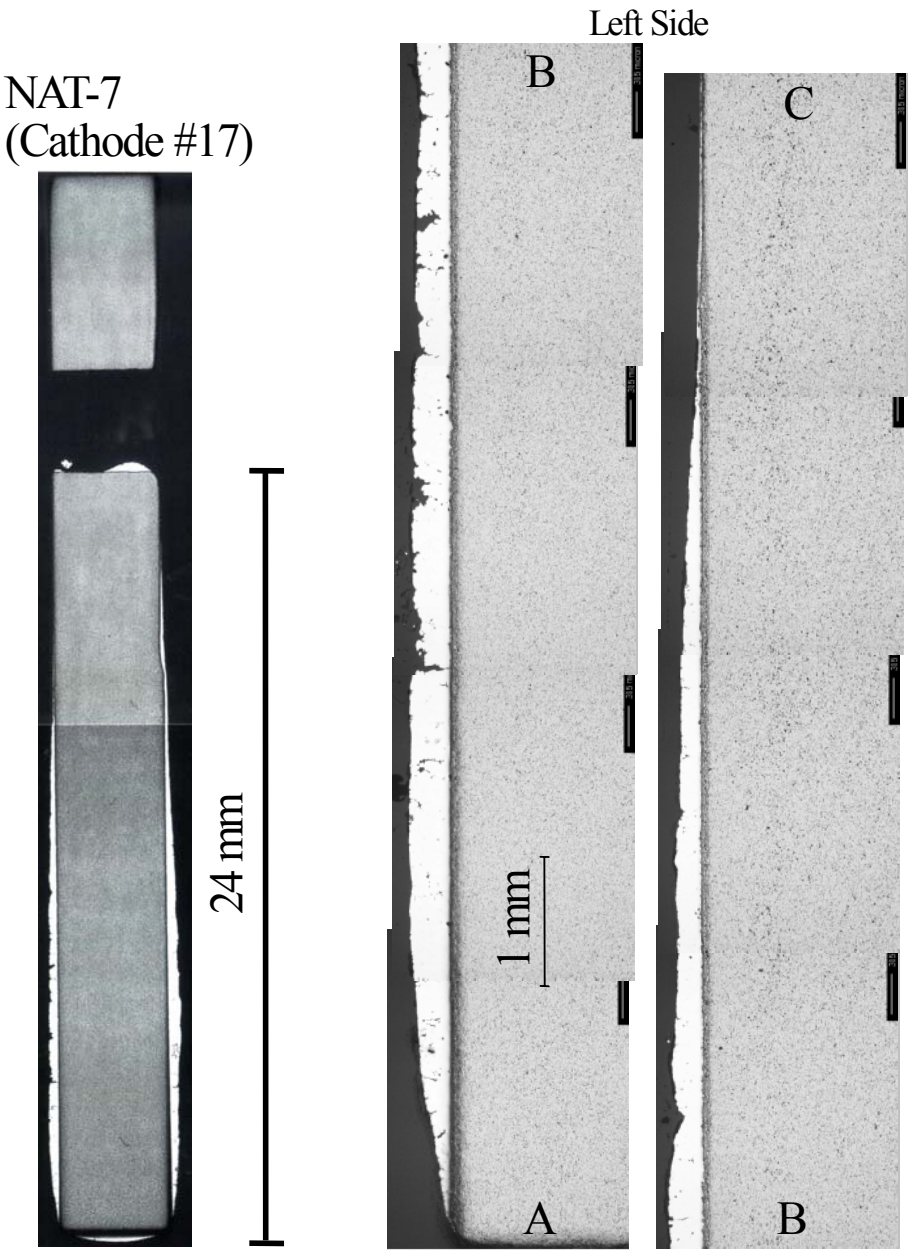

Figure A.20. Optical Images of NAT-7 at Different Magnifications Showing Al Layer over the Length of the Cathode Surface

NAT-7 (Cathode #17)

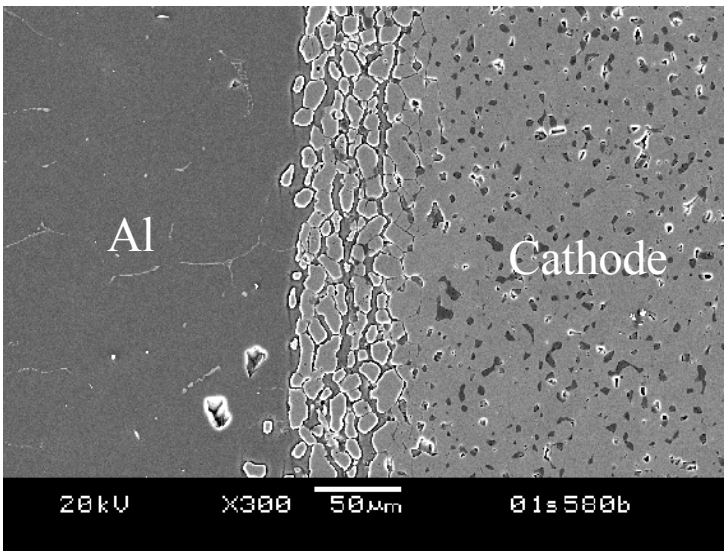

NAT-6 (Cathode #12)

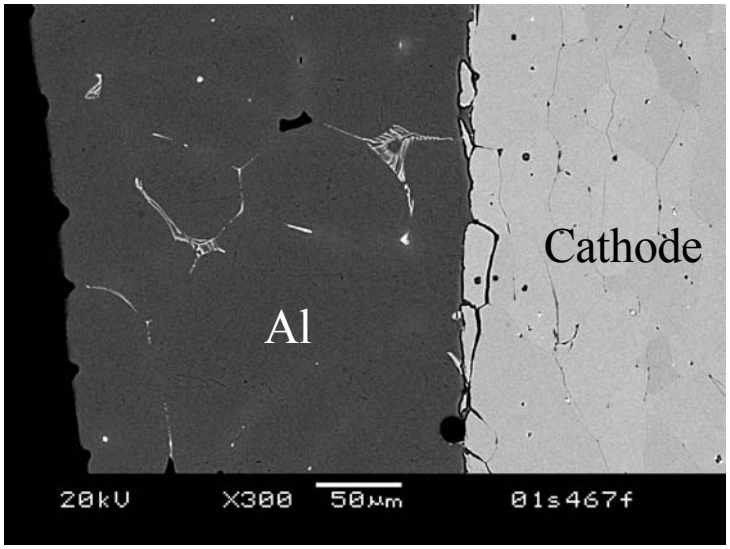

Figure A.21. SEM Image of Thick Region of Al Metal Layer on NAT-7

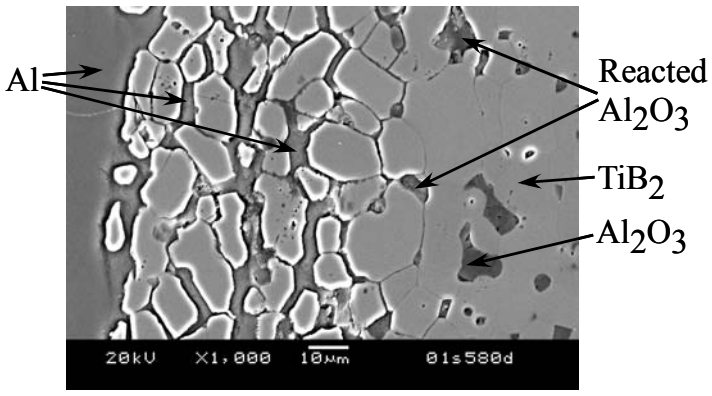

Figure A.22. Higher Magnification SEM Image of Surface of NAT-7 Showing Intergranular Corrosion

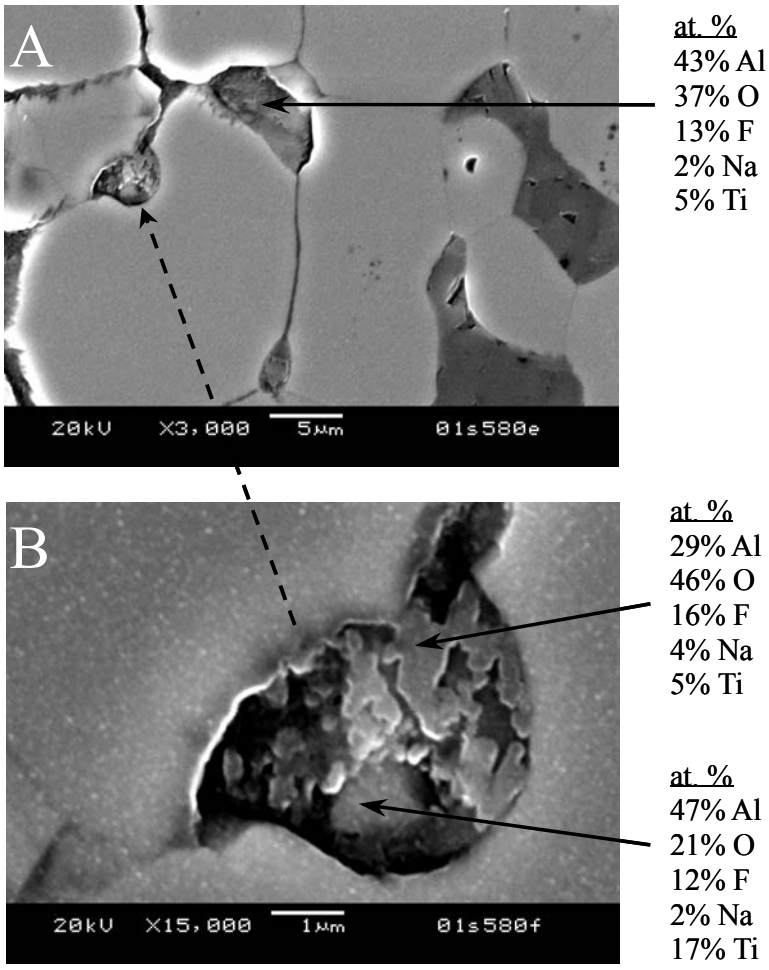

Figure A.23. Higher Magnification SEM Image of NAT-7 Showing Phases at Attacked Grain Boundaries

Bottom Edge

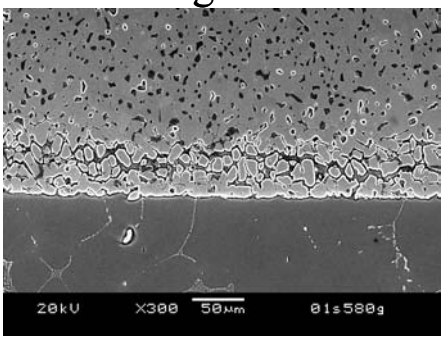

Corner

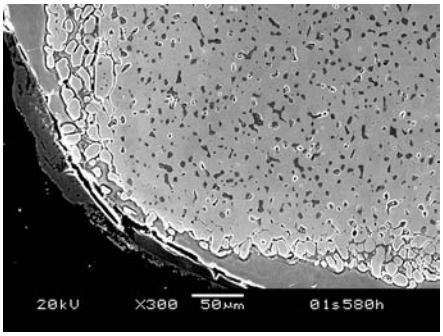

Figure A.24. SEM Images of Bottom Edge of NAT-7

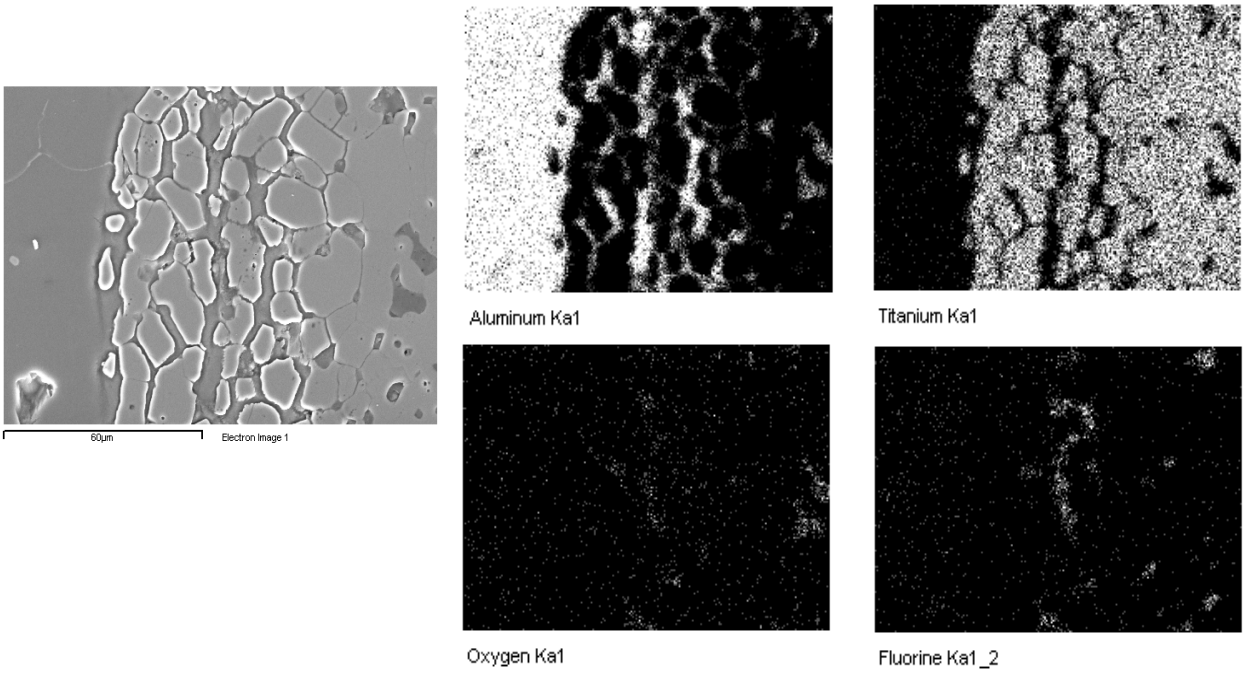

Figure A.25. Electron Dot Maps of NAT-7

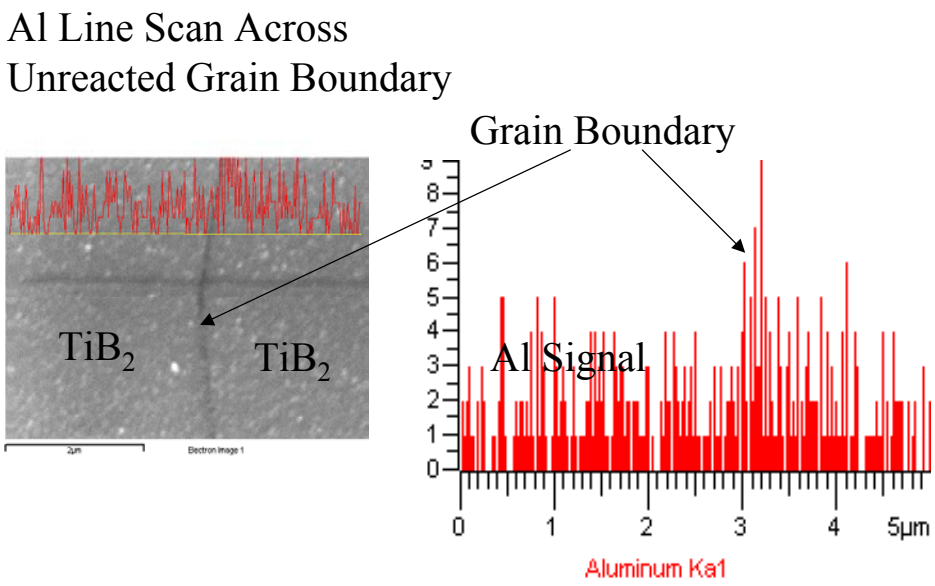

Figure A.26. Elemental Al Line Scan Across Uncorroded Grain Boundary in NAT-7

Bulk

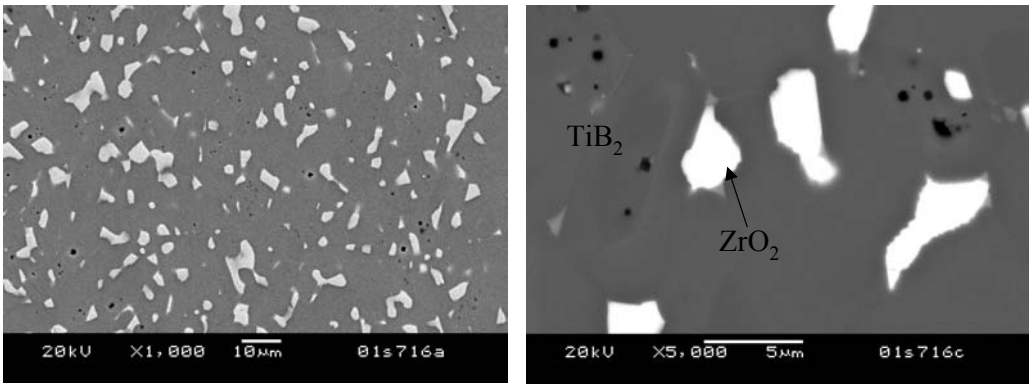

TiB_2 phase contains trace Zr, about 0.5 at.%.
ZrO_2 phase contains Ti, about 6 at.%.

Figure A.27. SEM Image of Bulk of NAT-8

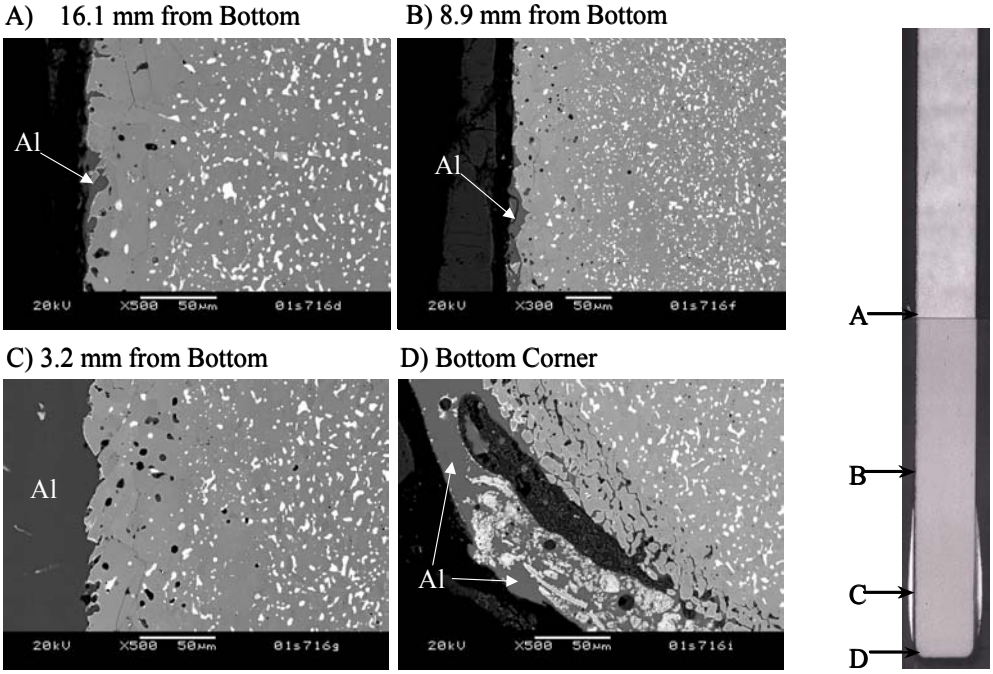

Figure A.28. Optical Image of Cross Section of NAT-8 with SEM/EDS Results Shown for Indicated Locations

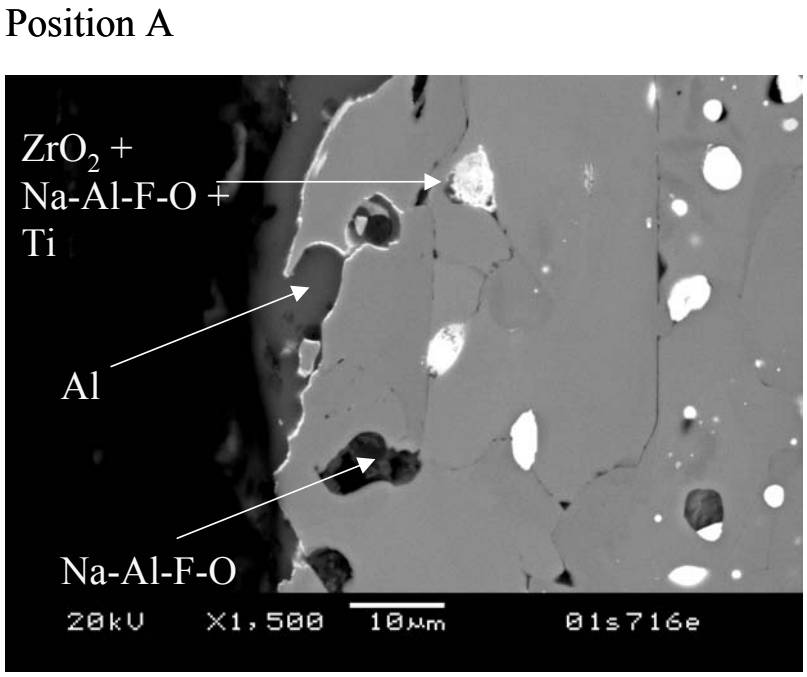

Figure A.29. SEM Image of Portion of NAT-8 in the Upper Regions Showing Attack by Electrolyte

Position C

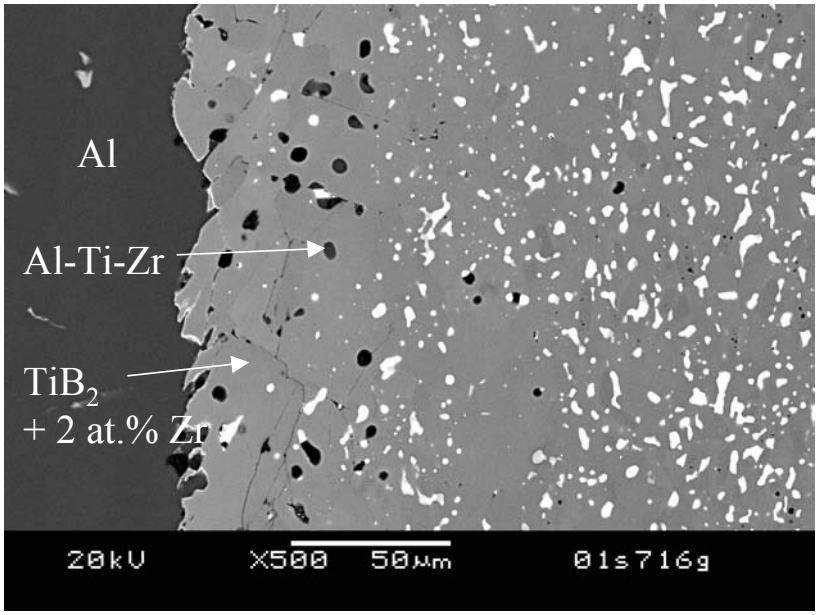

Figure A.30. SEM Image of Portion of NAT-8 Under the Thicker Al Layer with EDS Results

Position D

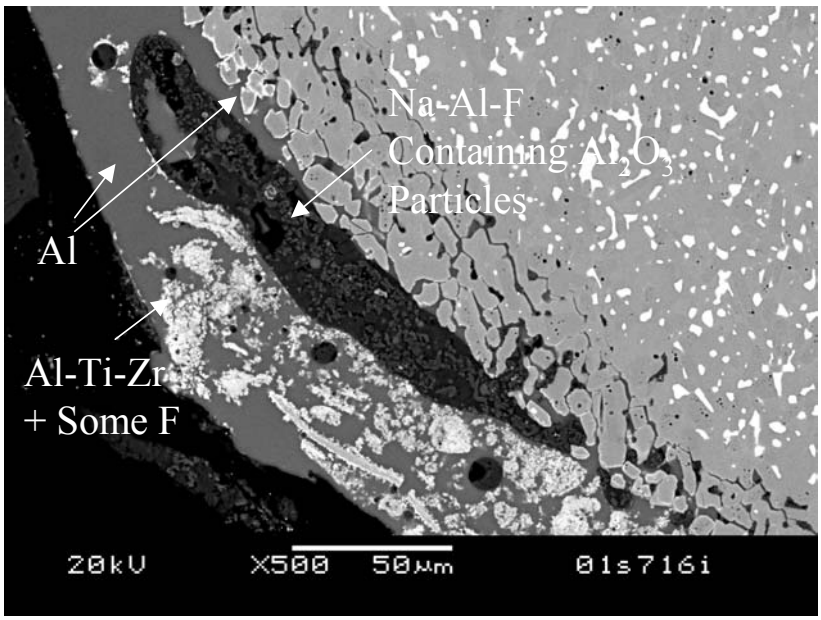

Figure A.31. SEM Image of Corner of NAT-8 Showing Significant Rounding

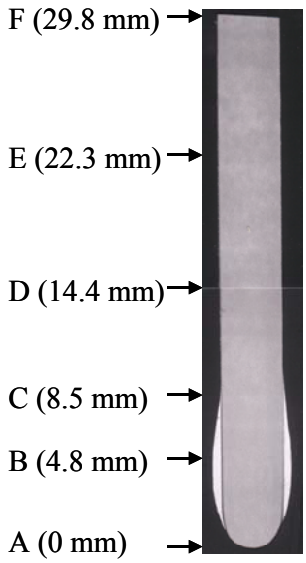

Figure A.32. Composite Optical Image of Cross Section of NAT-9 Showing Locations of SEM Images

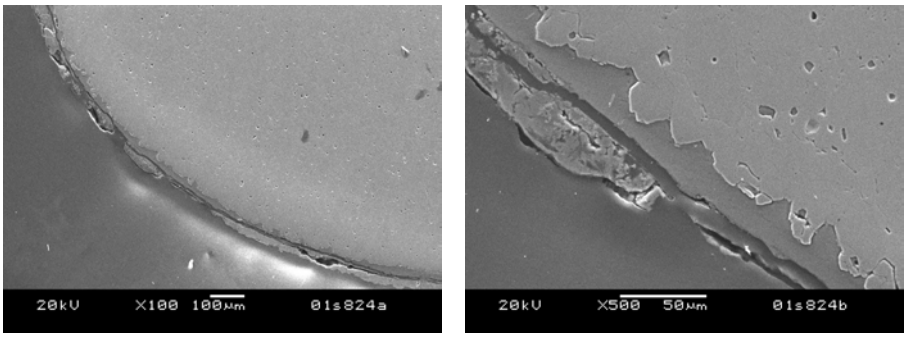

100X 500X

Figure A.33. SEM Image of NAT-9 at Position A

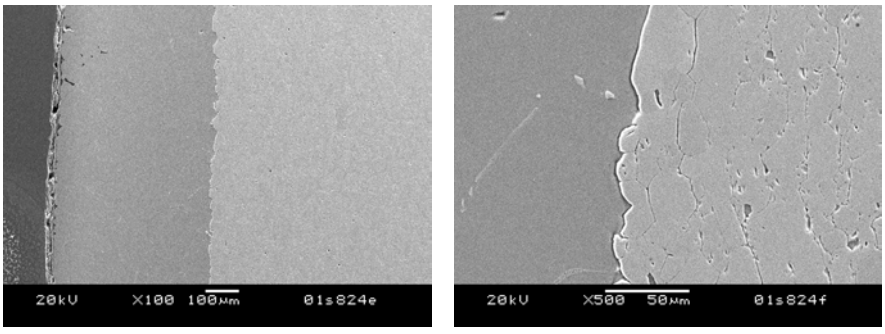

100X 500X

Figure A.34. SEM Image of NAT-9 at Position B

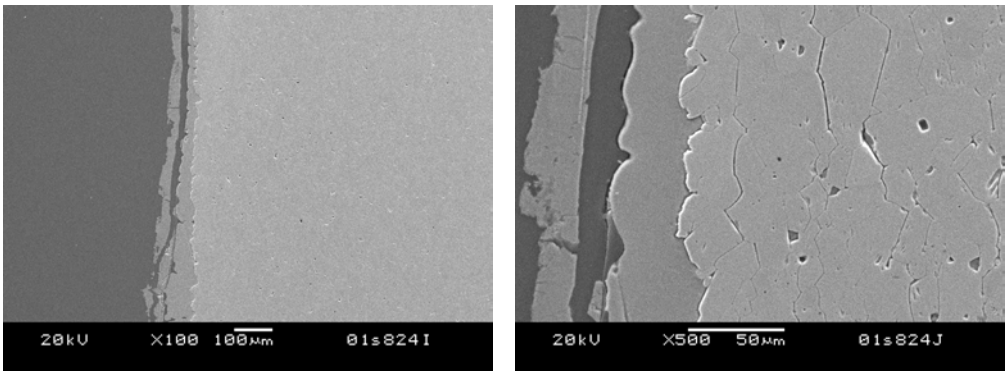

100X 500X

Figure A.35. SEM Image of NAT-9 at Position C

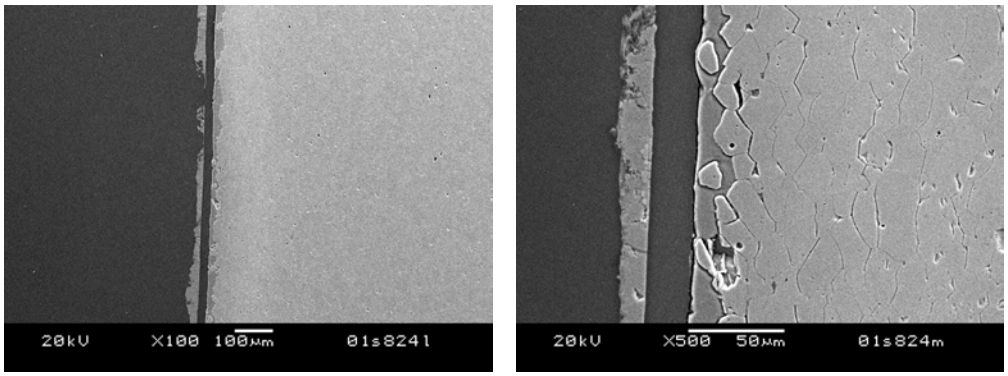

100X 500X

Figure A.36. SEM Image of NAT-9 at Position D

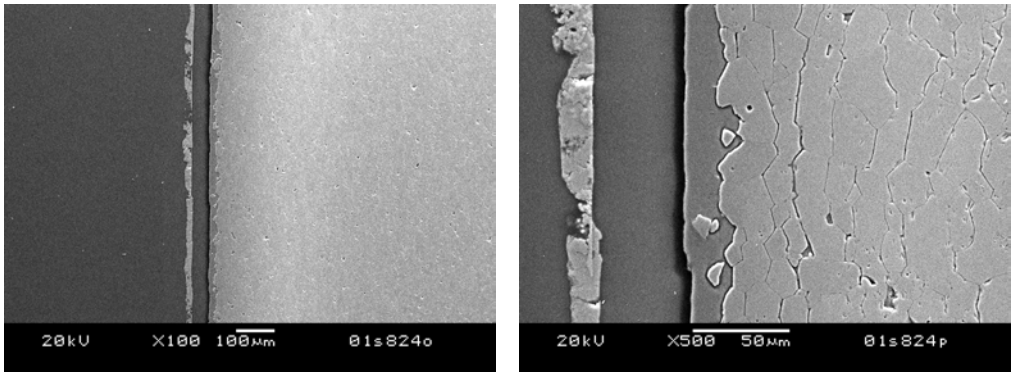

100X 500X

Figure A.37. SEM Image of NAT-9 at Position E

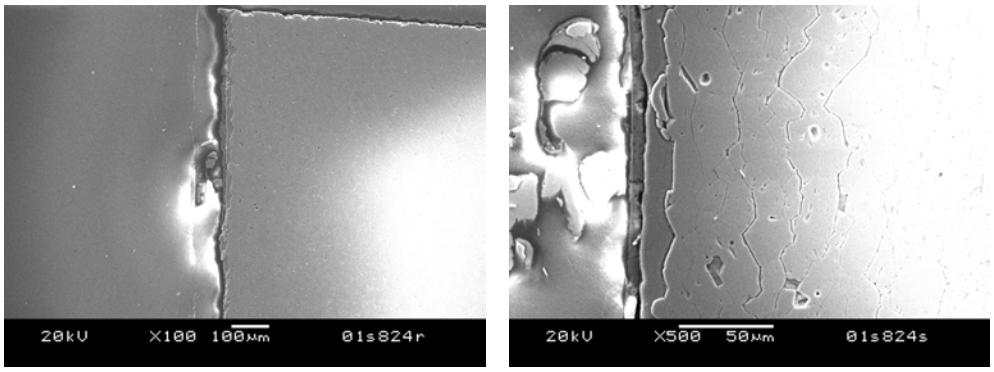

100X 500X

Figure A.38. SEM Image of NAT-9 at Position F

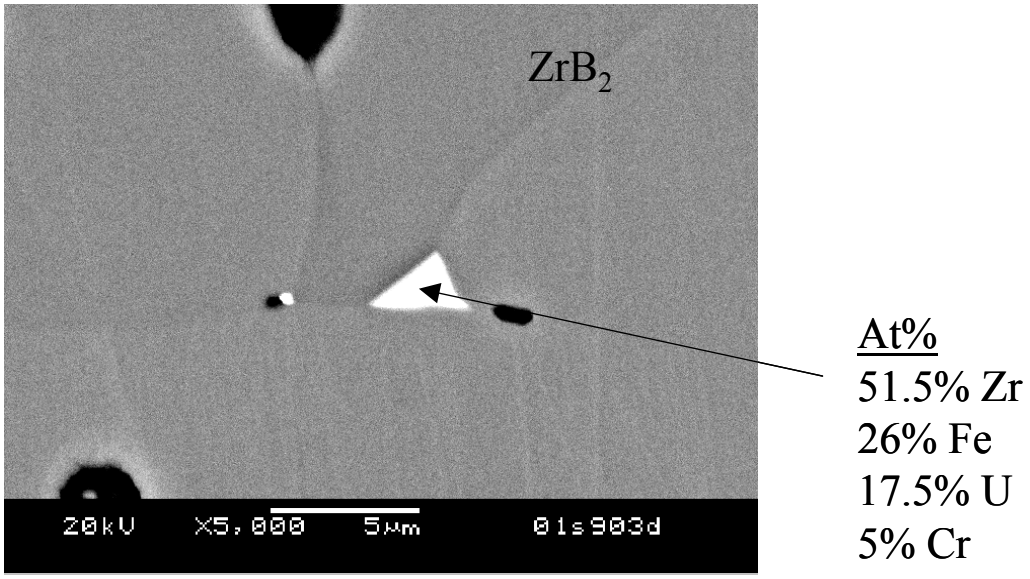

Figure A.39. SEM Image of Bulk of NAT-10 with EDS Results

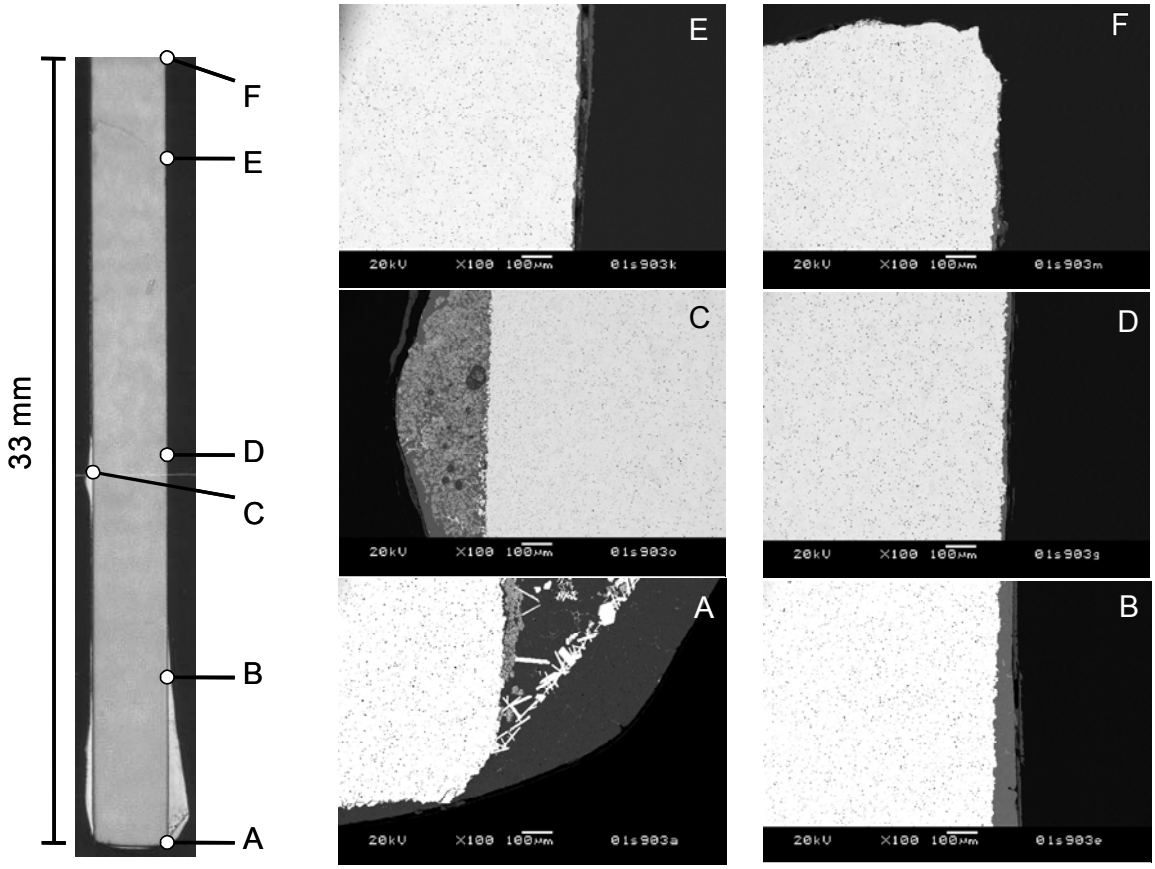

Figure A.40. Composite Optical Image of Cross Section of NAT-10 with SEM Images at Indicated Locations

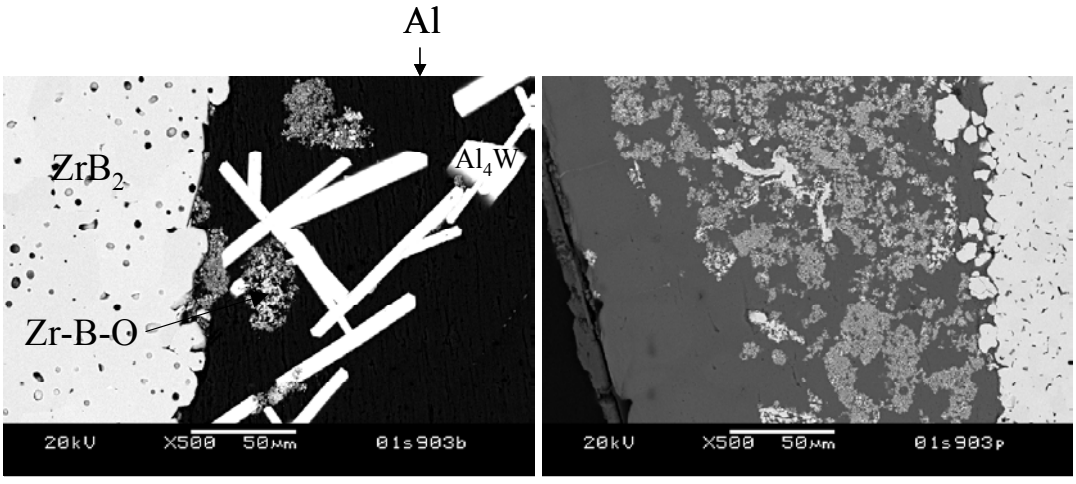

Figure A.41. SEM Images of NAT-10 with EDS Results Showing Al Metal at Different Locations

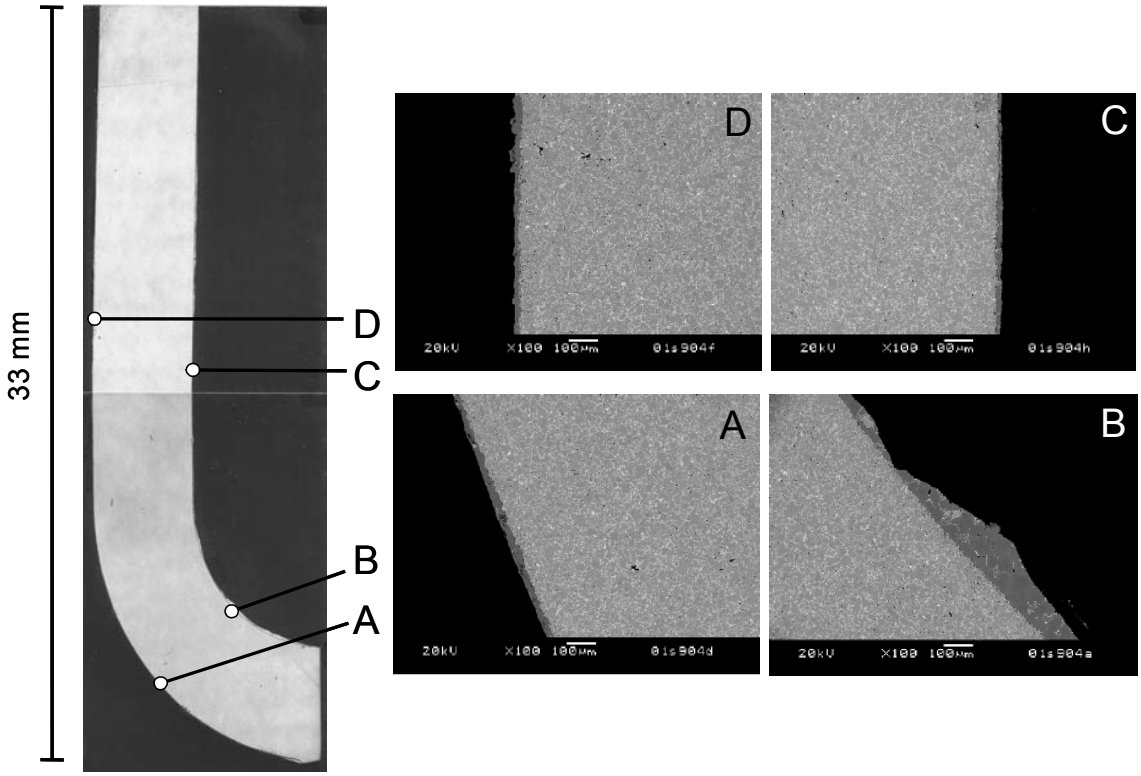

Figure A.42. Optical Microscopic and SEM Results on NAT-11

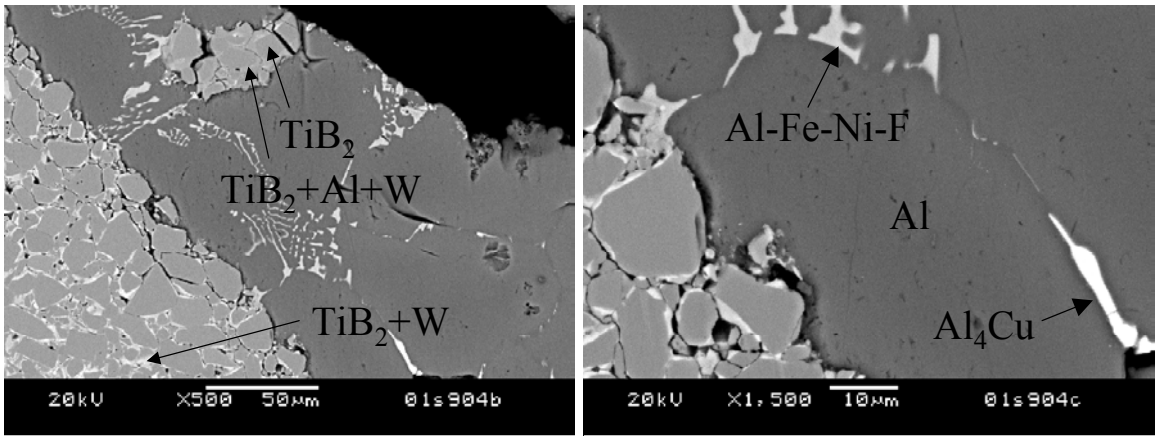

Figure A.43. SEM Images and EDS Results of NAT-11 Near Position B

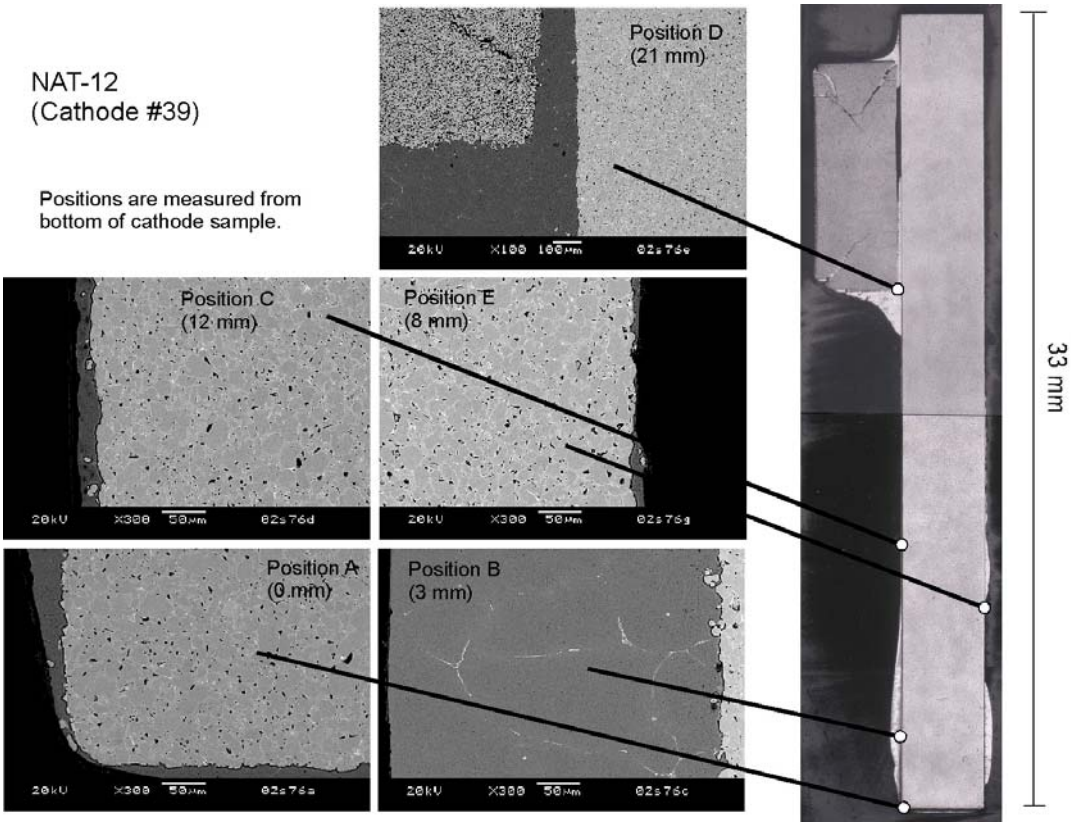

Figure A.44. Composite Optical Image of Cross-Section of NAT-12 with SEM Images at Indicated Locations

NAT-12
(Connector Material)

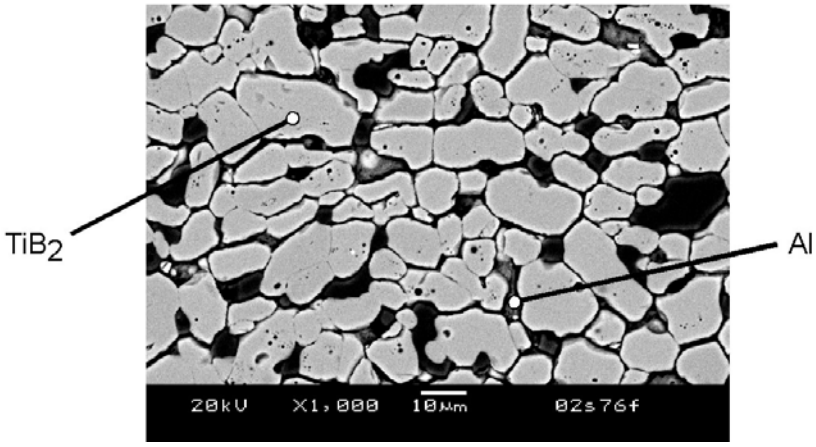

Figure A.45. SEM Image of Connector Material in NAT-12

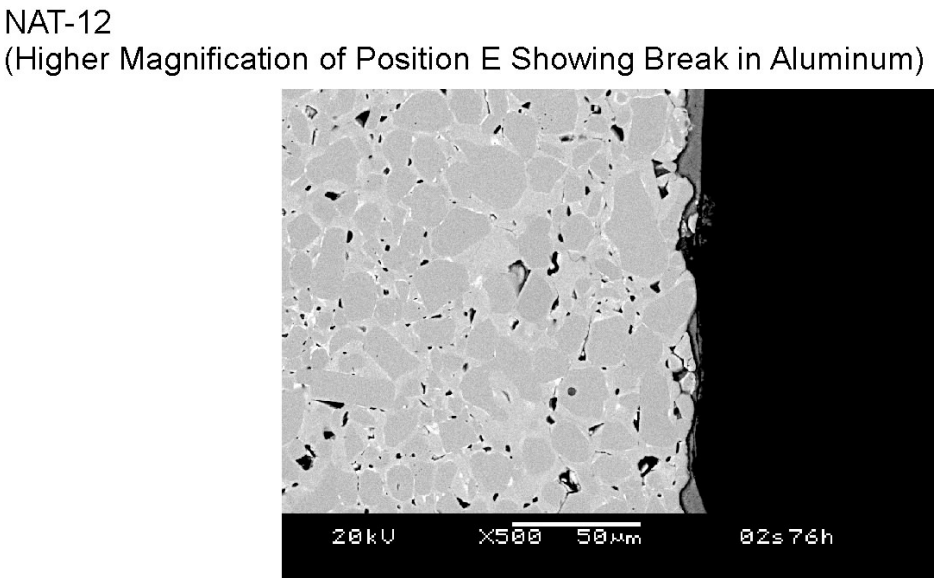

Figure A.46. Higher Magnification SEM Image of Position E in NAT-12 Showing Break in Al Metal Layer

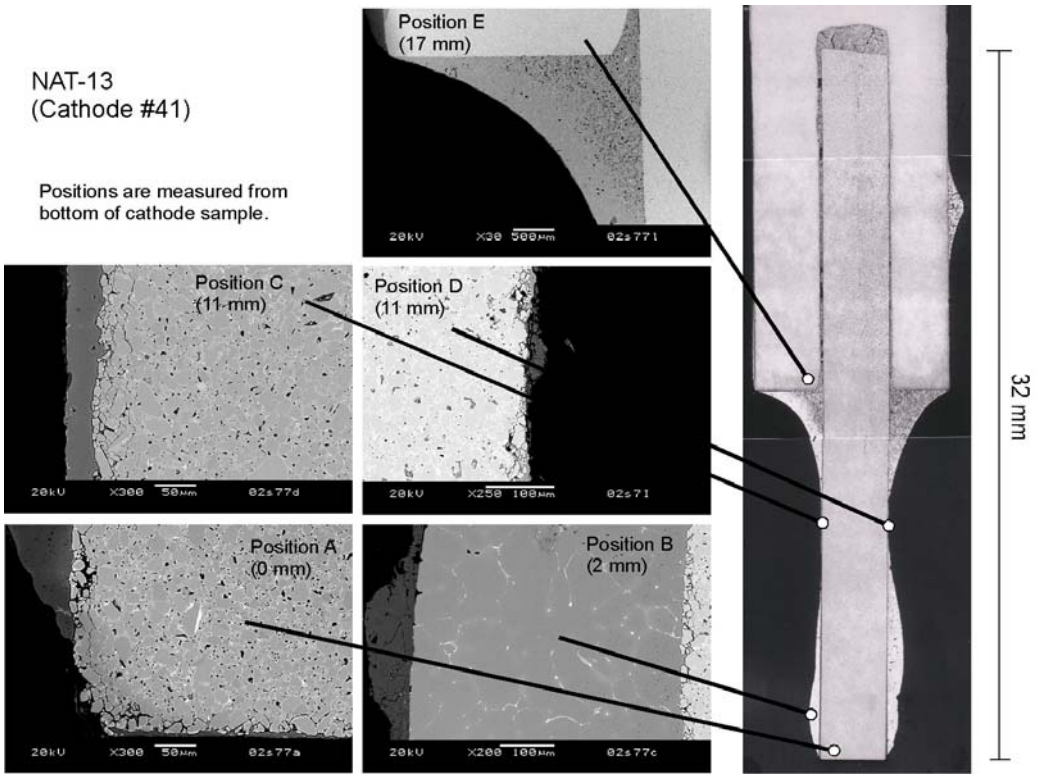

Figure A.47. Composite Optical Image of Cross Section of NAT-13 with SEM Images at Indicated Locations

NAT-13
(Higher Magnification of Connector Material)

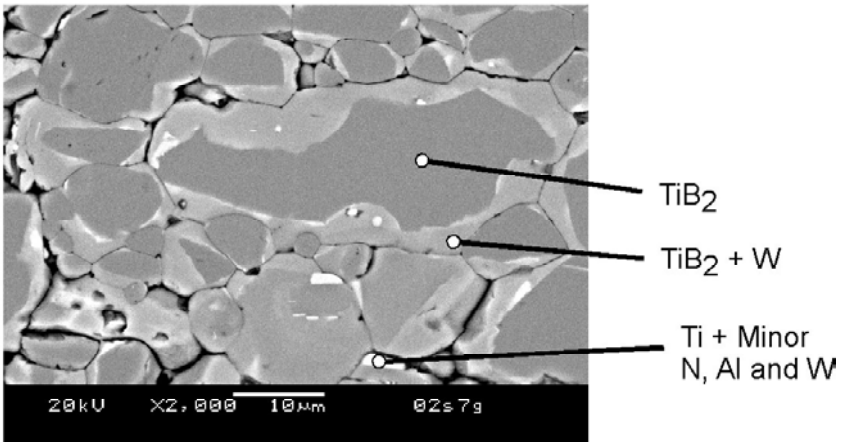

Figure A.48. SEM Image of Connector Material in NAT-13

NAT-13
(Higher Magnification of Region around Connector)

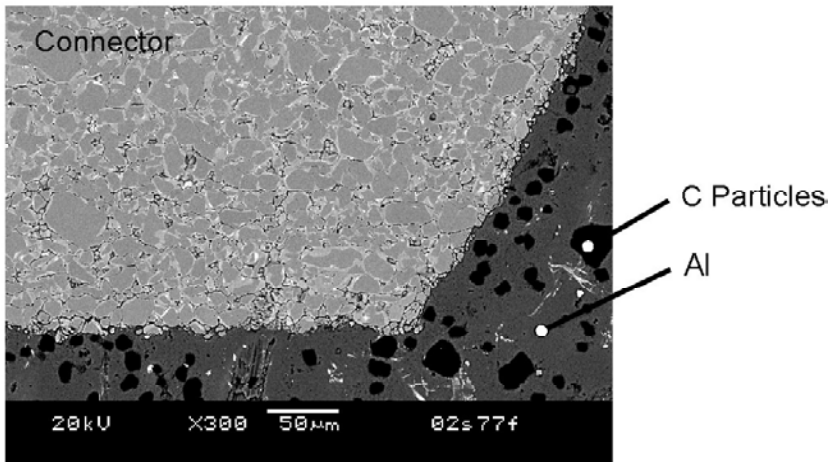

Figure A.49. SEM Image of Region Around Connector in NAT-13

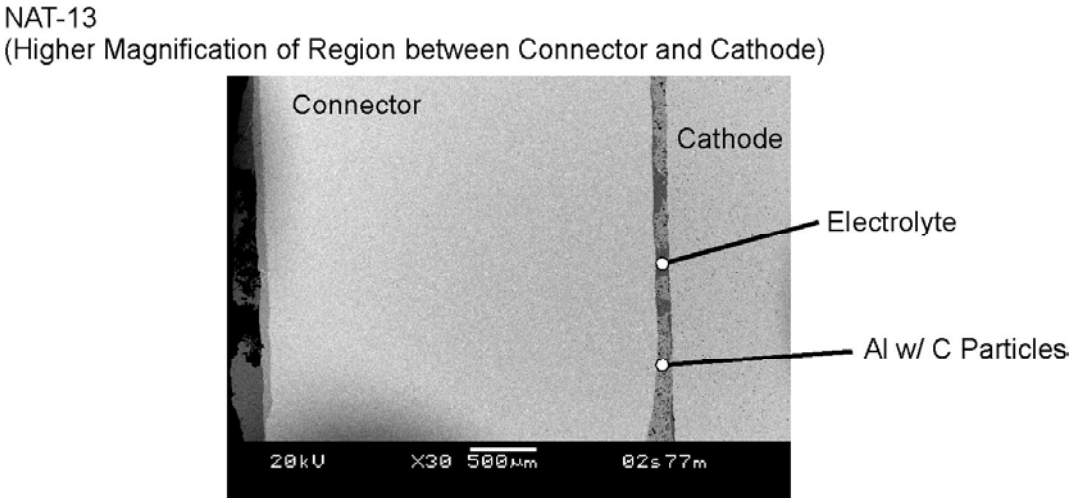

Figure A.50. SEM Image of Region Between Connector and Cathode in NAT-13

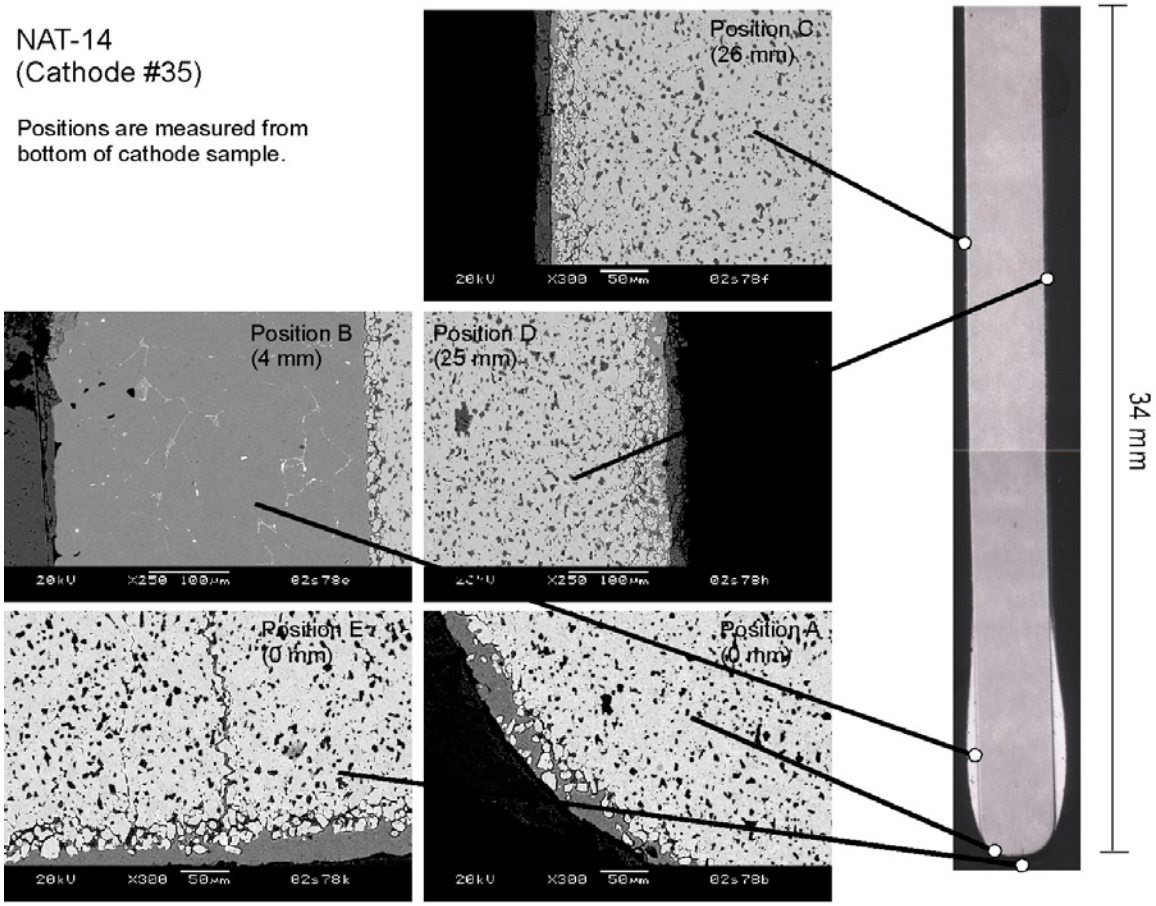

Figure A.51. Composite Optical Image of Cross Section of NAT-14 with SEM Images at Indicated Locations

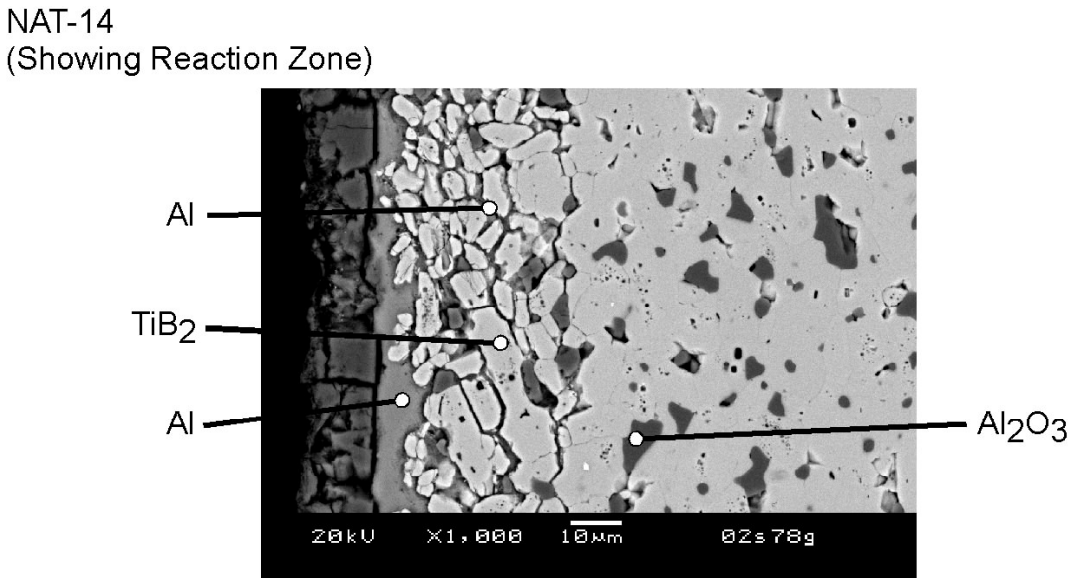

Figure A.52. SEM and EDS Results Showing Reaction Zone under Al Metal Layer in NAT-14

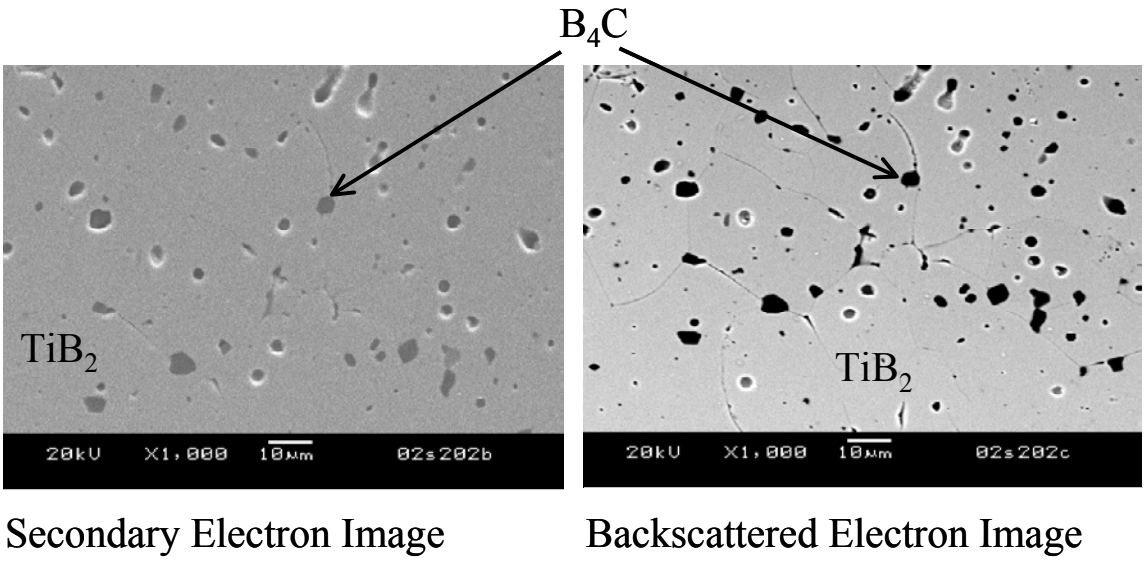

Figure A.53. SEM Image and EDS Results of the Bulk of NAT-15

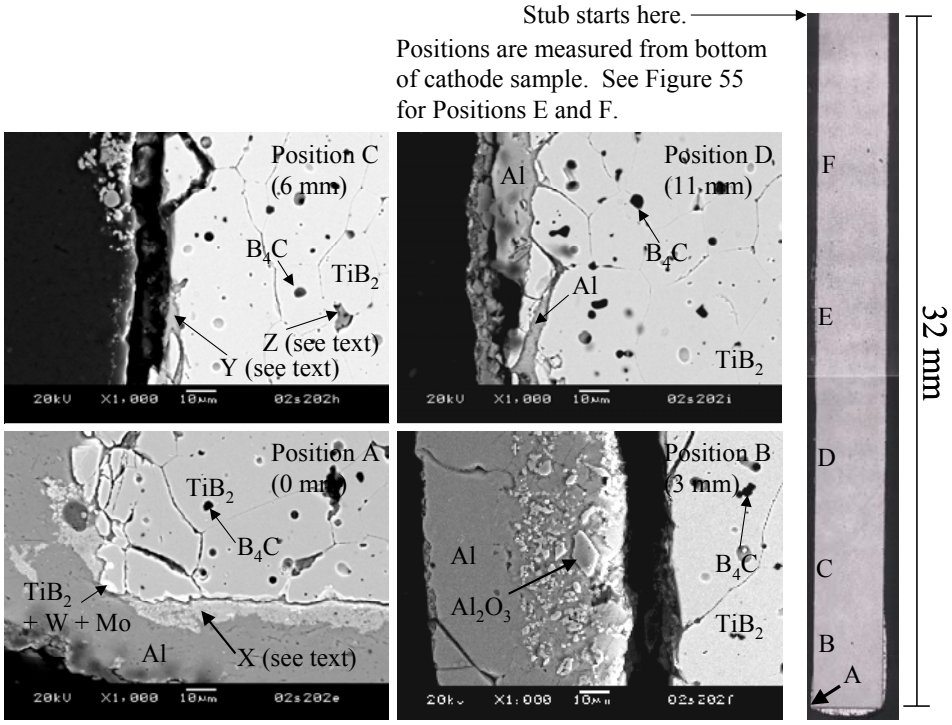

Figure A.54. Composite Optical Image of Cross Section of NAT-15 with SEM Images and EDS Results at Indicated Locations

Positions are measured from bottom of cathode sample. See Figure 54 to reference Positions E and F relative to other positions analyzed.

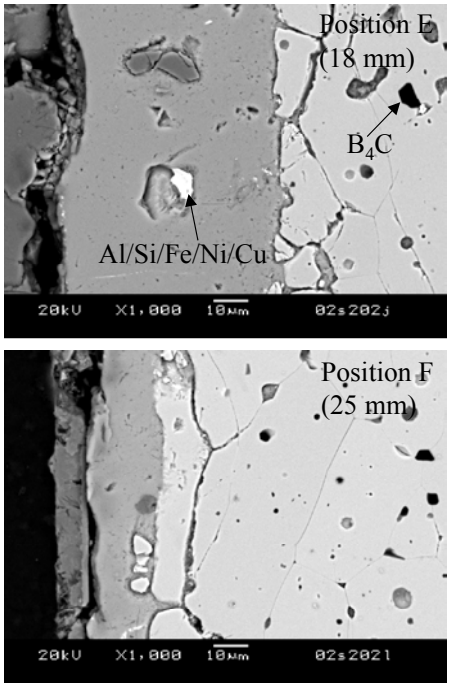

Figure A.55. Composite Optical Image of Cross-Section of NAT-15 with SEM Images and EDS Results at Indicated Locations (continued from Figure 54)

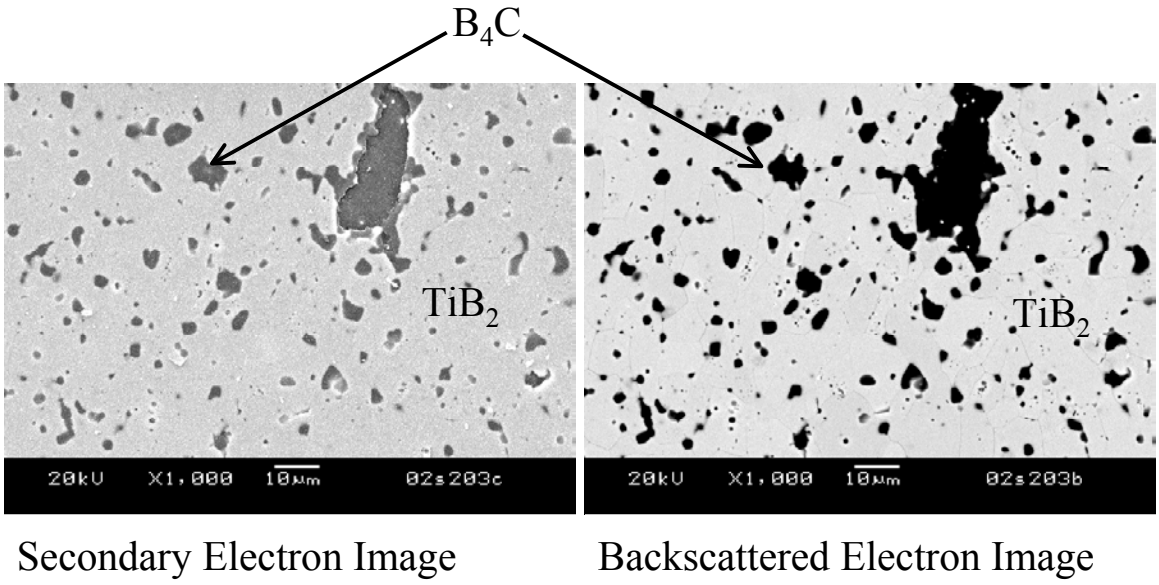

Figure A.56. SEM and EDS Results of Bulk Composition of NAT-16

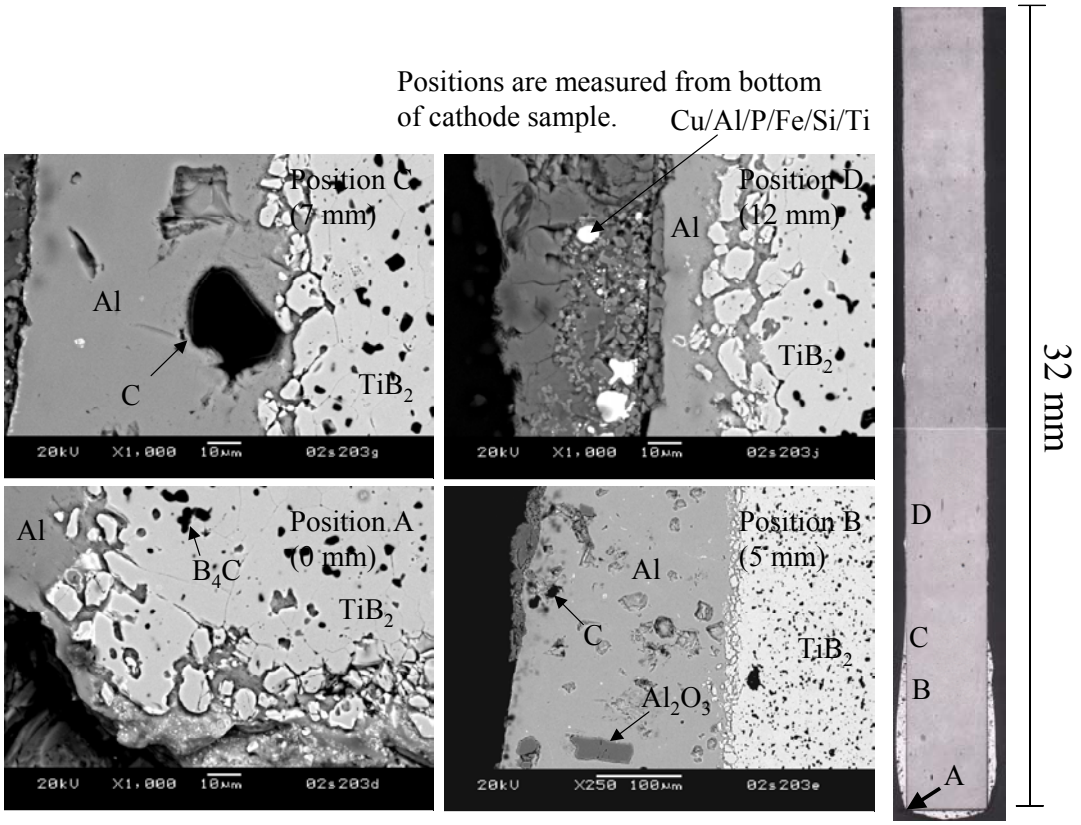

Figure A.57. Composite Optical Image of Cross Section of NAT-16 with SEM Images and EDS Results at Indicated Locations

Figure A.58. Composite Optical Images of Cross Sections of NAT-17, NAT-18, NAT-19, and NAT-20

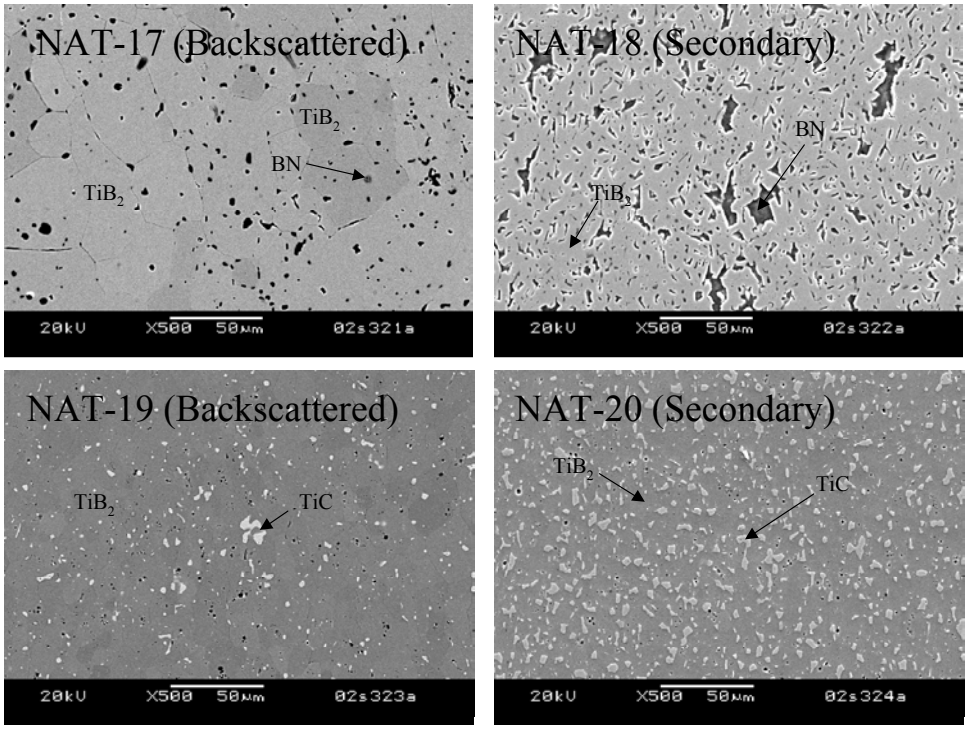

Figure A.59. Bulk Microstructure and Composition of NAT-17, NAT-18, NAT-19, and NAT-20

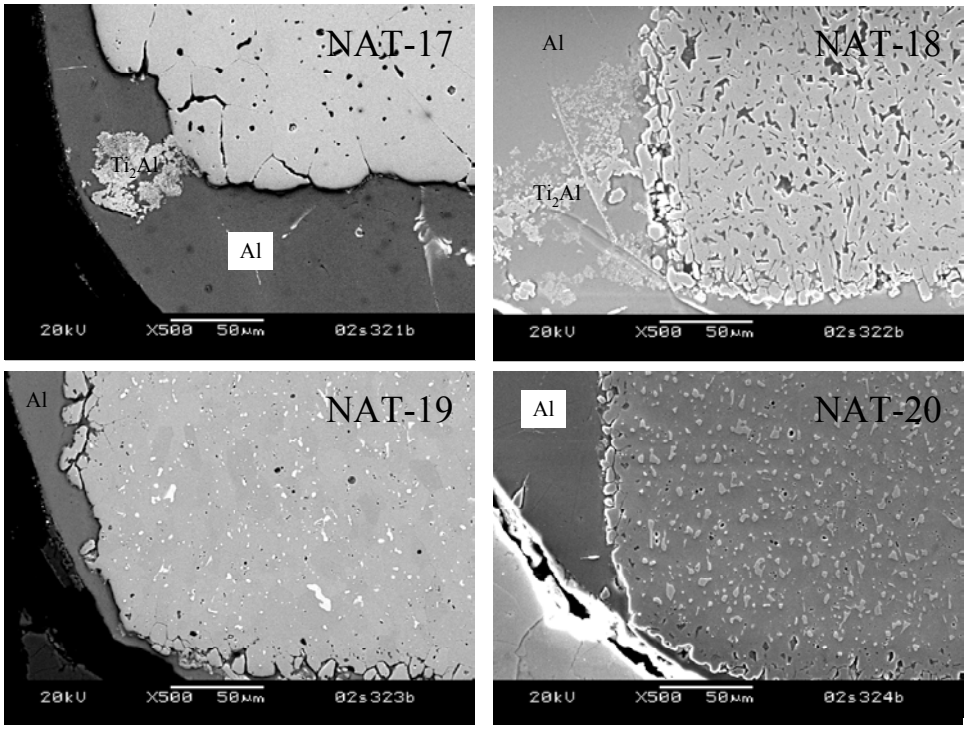

Figure A.60. Microstructure of Corners of NAT-17, NAT-18, NAT-19, and NAT-20

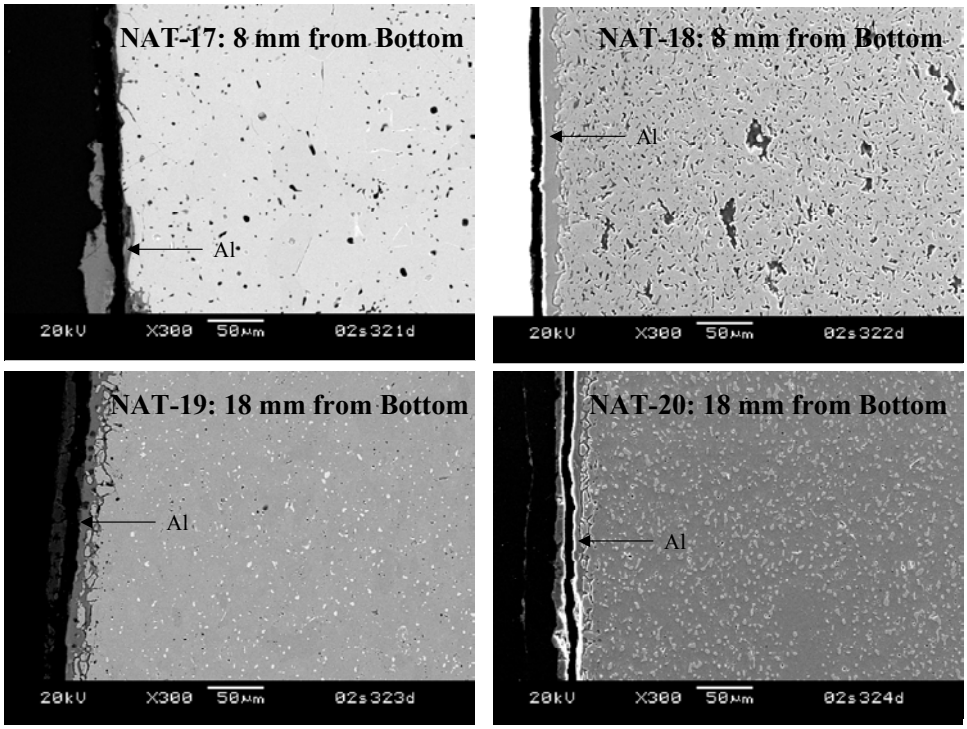

Figure A.61. Microstructure of Sides of NAT-17, NAT-18, NAT-19, and NAT-20

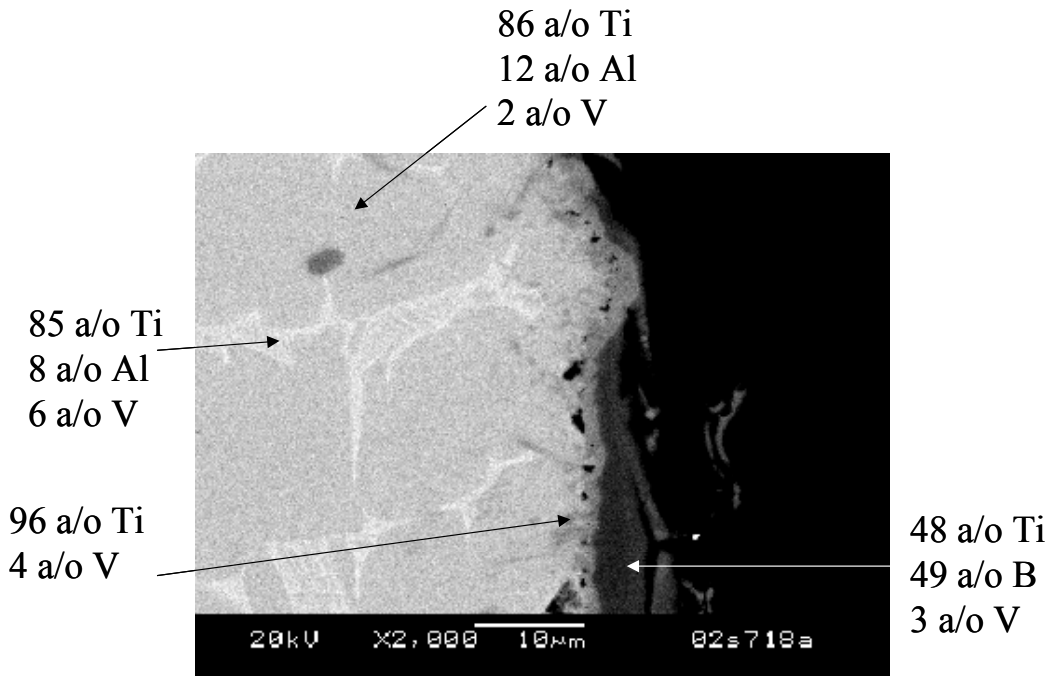

Figure A.62. SEM and EDS Analysis of NAT-21

Distribution

No. of Copies

OFFSITE

C. Brown
Northwest Aluminum Technologies, Inc.
1080 West Ewing Pl.
Ste. 202
Seattle, WA 98119

R. Roberts
c/o Craig Brown
Northwest Aluminum Technologies, Inc.
1080 West Ewing Pl.
Ste. 202
Seattle, WA 98119

T. Robinson
U.S. Department of Energy
Office of Industrial Technologies, EE-20
1000 Independence Ave, SW
Washington, DC 20585

J. Yankeelov
DOE-ID Operations Office
850 Energy Drive
Idaho Falls, ID 84301-1563

No. of Copies

ONSITE

23 Pacific Northwest National Laboratory

S. Baskaran	K2-44
S. Q. Bennett	K7-90
G. J. Exarhos	K2-44
M. A. Khalee	K2-18
G. L. McVay	K7-20
L. R. Pederson	K2-50
L. M. Peurrung	K2-50
N. T. Saenz	K2-50
M. T. Smith	P8-35
S. C. Weiner	BWO
K. Williams	K8-50
C. F. Windisch Jr. (10)	K2-44
Information Release (2)	K1-06